Contr. Atmos. Phys., May 1998, p. 223–248
0005-8173/98/02 0223-26 $ 3.00/0

Single-Scattering Properties of Complex Ice Crystals in Terrestrial Atmosphere

PING YANG AND K. N. LIOU

Department of Atmospheric Sciences, University of California at Los Angeles, Los Angeles, California 90095-1565, USA

(Manuscript received October 27, 1997; accepted January 06, 1998)

Abstract

Various ice crystal shapes including fernlike geometry, plates with dendritic extensions and with sectorlike and broad branches, fractal geometry, and aggregates, have been numerically defined on the basis of available observations. The surface roughness of ice crystals is also accounted for by specifying the facet-tilt distribution in terms of Gram Charlier series for the small facets of which the rough surface consists. These ice crystal geometries along with those defined in our previous studies may approximately represent the ice crystal shapes frequently observed in cirrus clouds. An improved Monte Carlo/ray-tracing method has been developed to compute the single-scattering parameters for these complex ice crystals. The polarization configurations of the localized waves associated with Fresnelian rays are comprehensively accounted for by the improved method in ray-tracing procedure.

Complex ice crystals, in particular, those with fernlike structures, scatter more energy in the angular region 2°–20° and in the lateral and backward directions than hexagonal ice crystals. The former ice crystal geometries normally produce smaller polarization values. In particular, a substantial reduction for the negative polarization associated with the backscattering is found as a result of the complex crystal geometries. The surface roughness of ice crystals incorporated into the single-scattering calculation tends to smooth out the scattering peaks corresponding to halos. The roughness also significantly reduces the backscattering. When a substantial roughness condition is imposed, the computed phase function and the polarization configuration of scattered light are essentially featureless.

A database of the single-scattering parameters of ice crystals at solar wavelengths covering 0.2–5 μm has been established for various ice crystal shapes and sizes. This database can be useful in the parameterization of the bulk radiative properties of cirrus clouds to account for the effects of ice crystal size distribution and the percentage of various crystal habits. By applying this database to cold and warm cirrus clouds, it is demonstrated that the scattering and absorption characteristics of these clouds depend on both the size distribution and the shapes of ice crystals.

1 Introduction

Cirrus clouds, being global and located high in the atmosphere (Bretherton and Suomi, 1983; Wylie and Menzel, 1989; Ackerman et al., 1988), have a profound impact on the terrestrial climate system through their radiative effect. For example, they substantially contribute to the diabatic heating in the upper troposphere over tropical region (Ramaswamy and Ramanathan, 1989). The influence of cirrus clouds on weather and climate processes of various scales, and the relevance of their microphysical and radiative properties to climate and climatic feedback have been identified as a major unsolved problem in climate research (Liou, 1986; Stephens et al., 1990). These clouds possess a number of unique features; in particular, they are composed of almost exclusively nonspherical ice crystals. The scattering and absorption properties of these ice crystals are fundamental to the study of the energy budget in the Earth-atmosphere system. In addition, the angular distribution and the polarization configuration of the sun light scattered by ice crystals are also critical to the development of reliable remote sounding techniques for the detection of cirrus clouds and the retrieval of their optical and microphysical properties. The significance of the nonsphericity of ice crystals has been recognized in remote sensing studies and

climate modeling (e.g., Minnis et al., 1994; Kinne and Liou, 1989; Mishchenko et al., 1996). In particular, Mishchenko et al. (1996) have shown that the use of a wrong ice crystal shape model in retrieving the optical thinkness of cirrus clouds from bidirectional reflectance measurements can lead to an underestimation or an overestimation of the actual optical thinkness by a factor that can exceed 3. It has been found that Mie theory may substantially overestimate the extinction efficiency of nonspherical ice crystals in comparison with experimental measurements (Yang et al., 1997). As articulated by Liou and Takano (1994), approximation of nonspherical ice crystals by using equivalent spheres is inadequate and often misleading.

The predominant sizes of ice crystals in cirroform clouds usually fall in the applicable regime of the geometric optics (GO) method. In the past two decades, the GO method in terms of the ray-tracing technique has been employed by a number of researchers to investigate the scattering characteristics of ice crystals (Wendling et al., 1979; Coleman and Liou, 1981; Cai and Liou, 1982; Takano and Jayaweera, 1985; Takano and Liou, 1989a,b; Rockwitz, 1989; Zhang and Xu, 1995). These efforts, however, studied only well defined hexagonal columns and plates. To solve scattering properties for more complex ice crystal geometries, Macke (1993) has applied the ray-tracing technique to compute the phase functions of polyhedral ice crystals by accounting for various orders sub-rays. Takano and Liou (1995) have further developed a hit-and-miss Monte Carlo/ray-tracing method to compute the complete scattering phase matrix for hallow columns, bullet rosettes, dendrites and capped columns, commonly observed in cirrus clouds. Iaquinta et al. (1995) have also applied the Monte Carlo/ray-tracing technique to compute the phase function for bullet rosettes that may be composed of as many as eight ice crystal bullets. Most recently, Macke et al. (1996) have investigated the phase function and the degree of linear polarization for various nonspherical crystal shapes including sectorlike and stellar plates, and polycrystals represented by triadic fractals.

Observations show that natural ice crystals largely vary in form. In addition to the ice crystal shapes presented in the aforementioned investigations, fernlike ice crystals, plates with dendritic extensions and broad branches, and ice crystals with attachments are frequently observed in both nature and laboratory (Nakaya, 1954; Magano and Lee, 1966; Ono, 1969; Hobbs, 1974). Bentley and Humphreys (1962) have published about 3000 photographs of ice crystals, which were taken by using the transmitted light through the ice crystals. Various crystal shapes have also been presented by Nakaya (1954) for both natural and laboratory ice crystals. The replicator data collected during the First ISCCP (International Satellite and Cloud Climatology Project) Regional Experiment (FIRE) show that a large number of ice crystals in cirrus cloud may be aggregates or polycrystals (e.g., Mitchell et al., 1996). Furthermore, the surface of ice crystals may not be perfectly smooth planar faces because of the collision and coalescence occurring in the process of ice crystal formation and growth. Rough surface of ice crystals has been observed in laboratory by using an electron microscope (Cross, 1968). To extend our knowledge about the scattering properties of ice crystals, there is a necessity to study the light scattering problems involving these complex geometries. In particular, a database of the scattering parameters for various ice crystal shapes and sizes is still void at this point, which is required in practice for developing a reliable parameterization of the bulk radiative properties of cirrus clouds with respect to size distribution and ice crystal habit. It should be pointed out that the fundamental investigation on light scattering by irregular and complex ice crystals is an important scientific issue not only because of its significance for practical applications in the studies of remote sensing and radiative transfer, but also because of our limited understanding of the physical process.

The present study focuses on the scattering properties of ice crystals at solar wavelengths for which geometric optics is applicable. Thus, we apply the Monte Carlo/ray-tracing technique to solve the scattering problems involving complex ice crystal geometries. For ice crystals with moderate size parameters, an improved geometric optics method (Yang and Liou, 1996b) is applied to compute their scattering phase matrix. In addition, the ray-by-ray integration algorithm developed by Yang and Liou (1997) is used to calculate the extinction and absorption cross sections. In Section 2, various complex ice crystal geometries are defined on the basis of observed shapes of ice crystals. In that section, we also define the rough geometry for ice crystal surface in conjunction with the light scattering calculation. In Section 3, we present an improved Monte Carlo/ray-tracing technique to resolve the scattering of light by complex ice crystals. Presented in Section 4 are the numerical results and discussions. Finally, conclusions are given in Section 5.

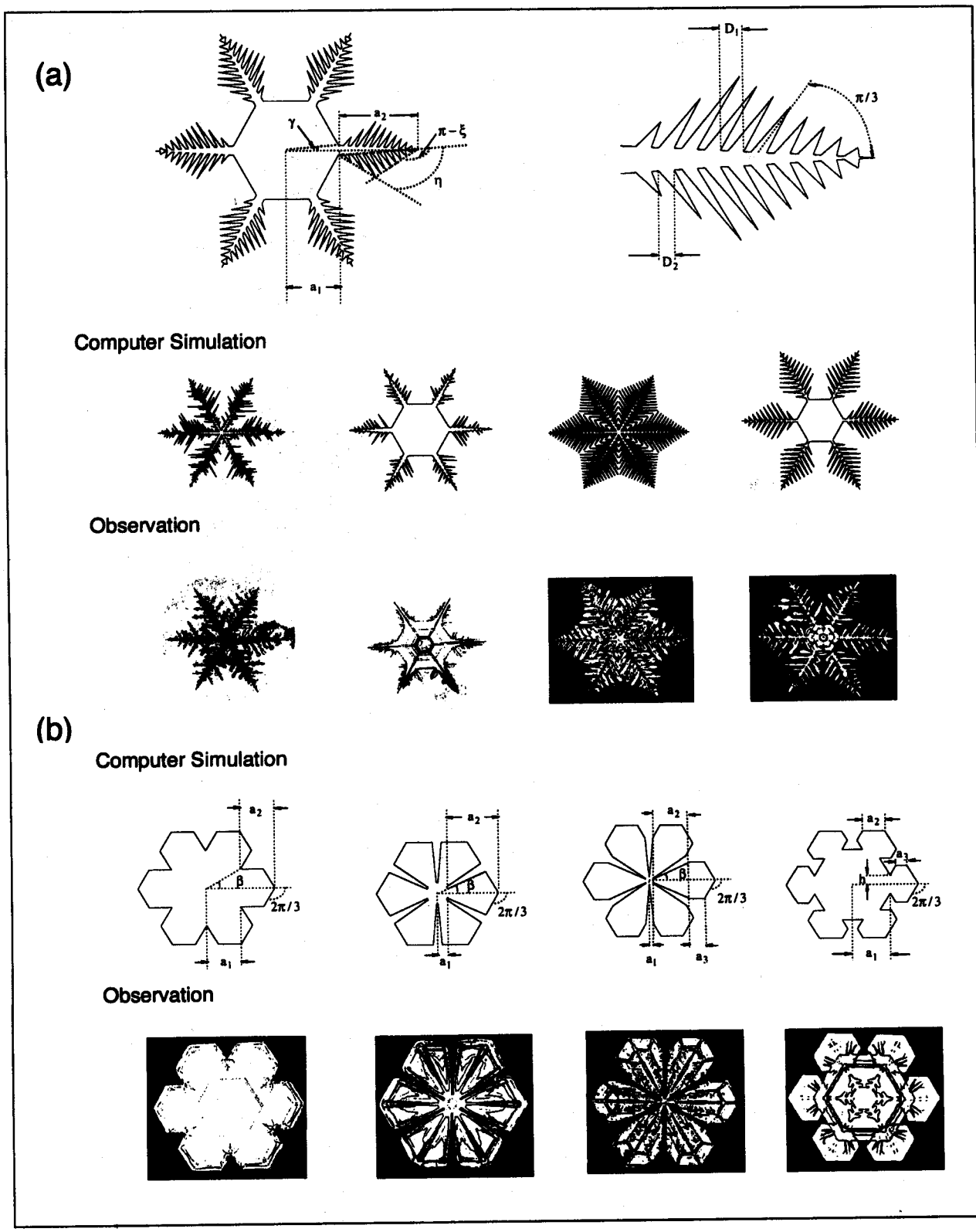

Figure 1: (a) Geometries for fernlike and dendritic ice crystals. (b) Geometries for ice crystals with broad and sectorlike branches.

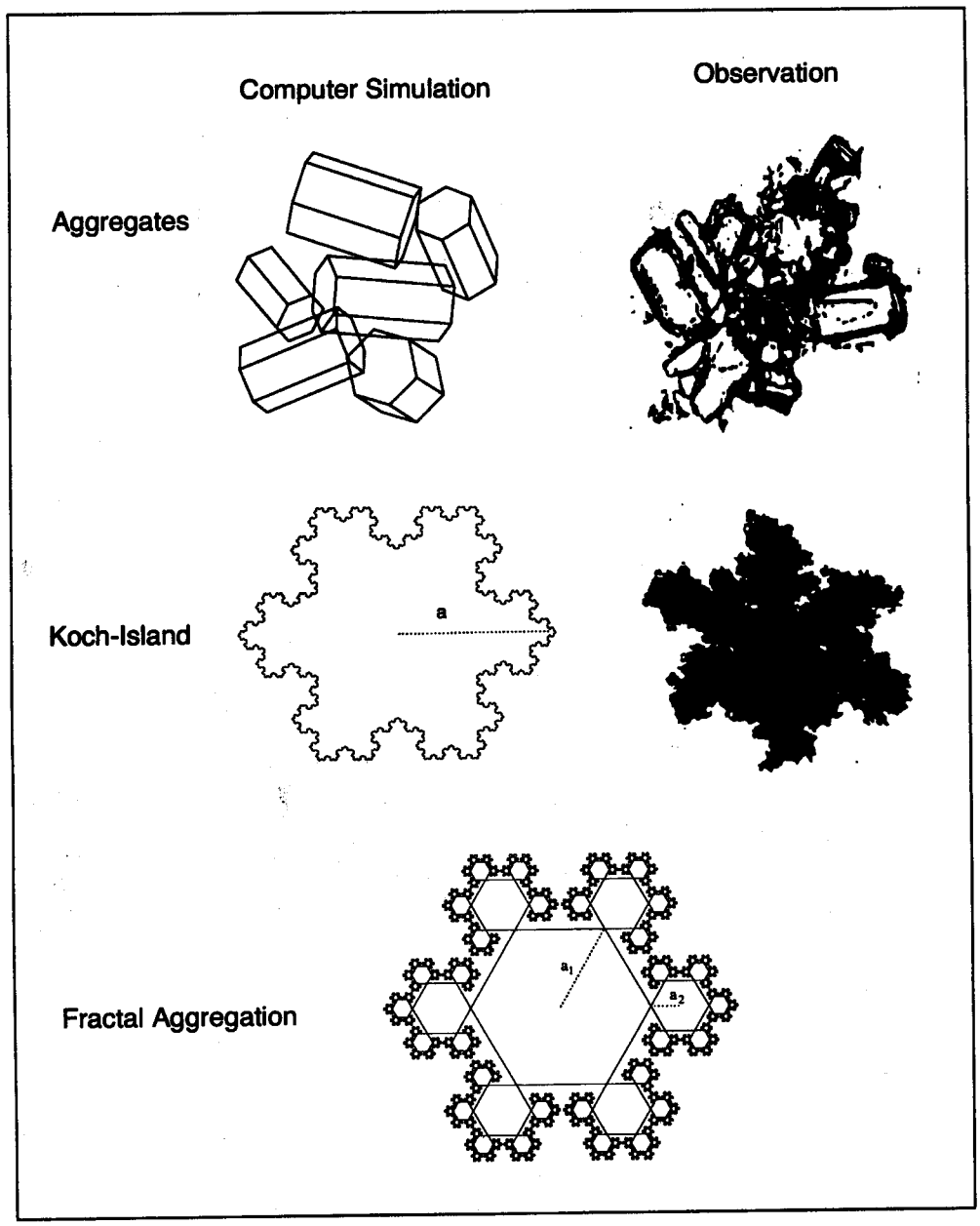

Figure 2: Geometries for aggregates and fractal ice crystals.

Table 1: The parameters associated with 8 hexagonal elements of which an aggregate consists. The listed semi-width, length, and element-center coordinates (x_o, y_o, and z_o) are given in a relative unit.

element #	semi-width	Length	γ' (°)	θ' (°)	φ' (°)	x_o	y_o	z_o
1	46.0	158.0	23.0	50.0	-54.0	0.0	0.0	0.0
2	40.0	124.0	16.0	81.0	156.0	15.808	105.189	-60.108
3	28.0	78.0	5.0	57.0	94.0	-26.691	73.005	47.369
4	48.0	126.0	13.0	76.0	130.0	-85.688	-39.19	-11.643
5	53.0	144.0	11.0	29.0	-21.0	104.532	33.08	27.801
6	19.0	54.0	8.0	62.0	-164.0	35.923	-49.692	-37.533
7	34.0	102.0	29.0	41.0	60.0	40.11	-57.227	110.238
8	43.0	138.0	19.0	23.0	-122.0	9.7524	-129.313	57.131

2 Complex Ice Crystal Geometries

The ice crystal geometries for fernlike ice crystals, plates with dendritic extensions, and plates with broad and sectorlike branches normally display a similarity of sixfold symmetry about their c-axis. Shown in Figure 1a are the geometries of the cross sections for fernlike ice crystals and plates with dendritic extensions. To define these ice crystal shapes, six major branches are extended from the corners of a hexagonal ice crystal (base ice crystal). The dimensions of the base ice crystal and the major branches are specified by two lengths, a_1 and a_2, and an angle, γ, as shown in the upper most panel of Figure 1a. A number of sub-branches are then extended from the six major branches. The total number of sub-branches on each major branch is denoted by $2N$. The contour enclosing the sub-branches on a major branch can be determined by two angles, η and ξ, as shown in the diagram. In the present study, the sub-branches are assumed to be equally spaced by a distance D_1 defined by

$$D_1 = \frac{a_2}{N+1}. \tag{2.1}$$

The widths of the sub-branches can be specified by

$$D_2 = \rho D_1, \tag{2.2}$$

where ρ, which is in the region of (0,1), is a parameter determining the widths of the sub-branches. To mimic the sub-branch lengths for natural ice crystals, we also simulate a random variation of the length for each sub-branch. For example, if b is the length of a sub-branch determined by the enveloping contour specified by the angles η and ξ, the randomly varied length, b', is then given as follows:

$$b' = \zeta b, \tag{2.3}$$

where ζ is a random number distributed uniformly in the region of (0,1). Note that different values of ζ are selected for non-identical sub-branches. According to the preceding procedure and selecting the aforementioned parameters properly, we can specify various shapes for fernlike crystals and plates with dendritic extensions. Shown in the second and third rows of Figure 1 are four examples of the numerically defined crystal geometries and the corresponding observed crystal shapes (Bentley and Humphreys, 1962; Nakaya, 1954). Note that the dendritic geometry defined by Takano and Liou (1995) is a special case of the present fern-like geometry.

Figure 1b shows computer generated and observed (Bentley and Humphreys, 1962) ice crystal geometries for another typical catalog of ice crystals including plates with broad and sectorlike branches and sprouts. In these diagrams the parameters that specify the ice crystal geometries are also defined. It is evident that the ice crystal geometries defined numerically are almost identical to those observed. However, inhomogeneous interior structures are evident for natural ice crystals. It is unlikely possible at this point to account for these inhomogeneous structures by applying the ray-tracing technique.

Aggregates have been frequently observed in the Earth's atmosphere. The diagrams in the first row of Figure 2 show an example for numerically defined and observed aggregate shapes (Kinne et al., 1994). For the numerically defined geometry, an aggregate is specified by properly selecting the spatial coordinates, dimensions, and aspect ratios of various hexagonal elements of which the aggregate consists so that these elements are attached together without overlap. Consider a hexagonal ice crystal element whose c-axis is parallel to the z-axis of a Cartesian coordinate system $oxyz$. The crystal can be rotated to any orientation by three consecutive coordinate transforms. First, the ice crystal is rotated by an angle, γ', about its c-axis. Then the c-axis is tilted from the z-axis by an angle, θ', in xoz plane. Finally, the c-axis is rotated about the z-axis by an angle, φ'. The spatial position of a specific element can be determined by the coordinate values of the particle center, x_o, y_o, and z_o. Table 1 lists the values of the preceding parameters for an aggregate composed of 8 hexagonal elements. The sizes and the center coordinates of the hexagonal elements are given in a relative unit, which can be scaled to obtain a proper dimension for an aggregate in the single-scattering calculation. The present light scattering computational program is capable of accounting for a various number of hexagonal elements attached in an arbitrary manner.

Fractal structures have been widely recognized in nature (Mandelbrot, 1982) and also in crystal formation under a fluctuating ambient condition (Witten and Sander, 1983). To understand the effect of the self-similar structures of ice crystal aggregations on single-scattering properties, Macke and Tzschihholz (1992) have computed the phase function for deterministic Koch-islands in an idealized two-dimensional (2-D) case, that is, the incident wave and scattering process are assumed to be confined on a 2-D plane. The cross-section geometry of a Koch-island plate with 5 generations is shown in the second row in Figure 2 along with an observed shape

(Magano and Lee, 1966). The constructing procedure for a Koch-island should not be explained in the present study because it can be found elsewhere (Mandelbrot, 1982; Vicsek, 1989). Since the 2-D scattering feature differs from its three-dimensional (3-D) counterpart, we have also applied the Monte Carlo/ray-tracing method to investigate the scattering characteristics of the ice crystals with Koch-island cross sections in the 3-D space. In addition, we have also studied the scattering of light by fractal crystal aggregations, whose geometry is also shown in Figure 2. To construct the aggregation geometry, a large hexagonal ice crystal (base ice crystal) of a semi-width a_1 is specified first. From the corners of the base ice crystal, six smaller hexagonal ice crystal sprouts with a semi-width a_2 are then extended and they are regarded as the second layer of the fractals. Similarly, the third layer crystals with a semi-width a_3 are attached to the second layer crystals at their corners. This procedure can be followed to construct higher order layers of the fractal aggregation. In the present study the aggregation is limited to 5 layers and the total number of ice crystals included in the aggregation is 937. It should be noted that the semi-widths of the ice crystal elements must be selected properly for each layer to avoid overlap.

Irregularly rough surface is evident from the observed ice crystal shapes shown in Figure 2. Rough structures of ice crystal surface have also been observed for single crystals and polycrystalline ice by using an electron microscope in laboratory (Cross, 1968), as shown by the electron micrographys in Figure 3a. To incorporate the surface roughness into the scattering calculation, we assume that a rough surface is composed of a number of small facets that are locally planar and randomly tilted from their positions corresponding to the case of smooth surface. As shown in Figure 3b, let the z-axis indicate the direction normal to the mean position of the particle surface as if the roughness is smoothed out. The tilt of a facet is determined by its normal direction that can be specified in terms of two angles, θ and φ. It can be proven that the slopes of a facet along the x- and y-direction are given as follows:

$$Z_x = \frac{\partial Z}{\partial x} = (\mu^{-2} - 1)^{1/2} cos\varphi, \tag{2.4}$$

$$Z_y = \frac{\partial Z}{\partial y} = (\mu^{-2} - 1)^{1/2} sin\varphi, \tag{2.5}$$

where $\mu = \cos\theta$. The derivatives in Eqs. (2.4) and (2.5) are confined on the facet. Based on *in situ* observations, Cox and Munk (1954) have found that

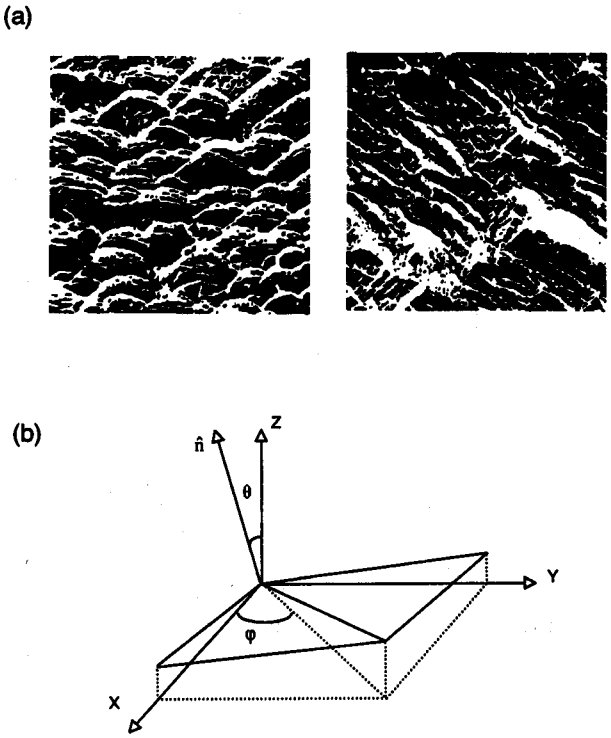

Figure 3: (a) Surface roughness of ice crystals observed by using a scanning electron microscope (after Cross, 1968). (b) The geometry for the tilt of a small facet on rough surface.

the roughness of wavy sea surface can be parameterized in terms of Gram Charlier series with fitting parameters depending on wind speed and direction. Since there are no sufficient quantitative experimental data about the roughness of ice crystal surface at this point, we assume that irregular roughness of ice crystal surface can also be specified by Gram Charlier distribution. If the tilt distribution of the roughness is azimuthally homogeneous (i.e., independent of angle φ), the statistical probability density for the condition that the slopes of a facet along the two axis directions are Z_x and Z_y is given by the first order Gram Charlier or a 2-D Gaussian distribution as follows:

$$P(Z_x,Z_y) = \frac{1}{\pi\sigma^2} exp[-(Z_x^2 + Z_y^2)/\sigma^2], \tag{2.6}$$

where σ is a parameter determining the magnitude of roughness. We note that σ=0-0.005, 0.005-0.05, 0.05-0.2 correspond to slight, moderate, and deep roughness in the single-scattering calculation, respectively. According to the geometry shown in Figure 3b and the probability distribution defined in Eq. (2.6), the random tilts of the small facets of

which the rough surface consists can be specified in a stochastical manner as follows:

$$\mu = 1/(1-\sigma^2 ln\eta_1)^{1/2}, \tag{2.7}$$

$$\varphi = 2\pi\eta_2, \tag{2.8}$$

where η_1 and η_2 are random numbers distributed uniformly in the region of (0,1). For each facet, new values are selected for the two random numbers. Once the tilt of each facet on the rough surface is determined, the roughness geometry for ice crystal surface is defined for the ray-tracing calculation. The single-scattering properties of the particles that are stochastically deformed have also been investigated by Peltoniemi et al. (1989), Muinonen et al. (1996), Macke et al. (1996), and Takano (personal communication). In particular, it should be pointed out that the present method accounting for the effect of rough surface is similar to that developed by Macke et al. (1996) who used a model of hexagonal ice crystals with randomly tilted facets. Since the ray-tracing technique is used in both methods, which is independent of whether the microfacets or the facets are tilted, the results obtained from the two methods should be similar.

3 Improved Monte Carlo/Ray-Tracing Algorithm

The conceptual principle for the present Monte Carlo/ray-tracing algorithm follows that employed by Takano and Liou (1995). The deterministic Fresnelian interactions between rays and particle surface (reflections and refractions) are treated as a number of stochastic events. When a ray hits particle surface, a reflection criterion based on Fresnel coefficients is evaluated to determine whether reflection or refraction occurs. However, in the previous algorithm a mean reflectance is used as the criterion, which is defined by

$$r = (|R_l|^2 + |R_r|^2)/2, \tag{3.1}$$

where R_l and R_r are the Fresnel reflection coefficients for the electric fields that are parallel and perpendicular to the incident plane, respectively. Because the ratio of the two field components differs for sequential reflections/refractions in the ray-tracing calculation, the effect of the ray polarization configurations on the determination of ray-paths is neglected if the preceding mean reflectance is applied. In addition, the mean reflectance determined by Eq. (3.1) cannot accurately account for the polarization configurations of reflected and refracted rays in the computation of the phase matrix. To circumvent these disadvantages, there is necessity to formulate the amplitude scattering matrix and to derive a proper reflection criterion in conjunction with the implementation of the Monte Carlo/ray-tracing technique.

Consider an incident ray propagating along the z-axis of a Cartesian coordinate-system, xyz. The polarization of the electric field associated with the ray can be specified by the directions along the x- and y-axis. If the ray is scattered along the direction indicated by a unit vector, $\hat{r}$, after the ray interacts with an ice crystal, the direction perpendicular to the scattering plane can be specified by

$$\hat{\beta} = \hat{r} \times \hat{z} / |\hat{r} \times \hat{z}|, \tag{3.2}$$

where the hat symbols indicate that the underlay quantities are unit vectors. When $\hat{r}$ is along the exact forward scattering ($\hat{z}$) or backward scattering ($-\hat{z}$), the scattering plane is not unique and $\hat{\beta}$ can be an arbitrary unit vector confined on the oxy plane in this case. The unit vector parallel to the scattering plane can be specified by

$$\hat{\alpha} = \hat{r} \times \hat{\beta}. \tag{3.3}$$

By using the two directions determined by Eqs. (3.2) and (3.3), scattered field with any polarization configuration can be expressed in terms of the two components that are parallel and perpendicular to the scattering plane, respectively.

To account for the polarization of field properly, let us consider two cases of incident polarization configurations for the ray-tracing calculation. First, let the incident electric field be polarized along the x-axis. The scattered field associated with an outgoing or scattered ray, which is decomposed with respect to the scattering plane, can be indicated by

$$\begin{pmatrix} E^s_{\alpha,1} \\ E^s_{\beta,1} \end{pmatrix} = \begin{pmatrix} E^s_{\alpha} \\ E^s_{\beta} \end{pmatrix} \Bigg|_{\substack{E^i_x = 1 \\ E^i_y = 0}}, \tag{3.4}$$

where the superscripts i and s denote the incident and scattered fields, respectively; the subscripts α (or β) and x (or y) denote the polarization directions for the scattered and incident fields, respectively. Similarly, if the incident polarization is along the y-axis, we indicate the corresponding scattered field as follows:

$$\begin{pmatrix} E^s_{\alpha,2} \\ E^s_{\beta,2} \end{pmatrix} = \begin{pmatrix} E^s_{\alpha} \\ E^s_{\beta} \end{pmatrix} \Bigg|_{\substack{E^i_x = 0 \\ E^i_y = 1}}. \tag{3.5}$$

According to the definition of the amplitude scattering matrix **S** (van de Hulst, 1957), we obtain the following expression:

$$\mathbf{S} = \begin{pmatrix} S_2 & S_3 \\ S_4 & S_1 \end{pmatrix}$$

$$= f \begin{pmatrix} E^s_{\alpha,2} & E^s_{\alpha,1} \\ E^s_{\beta,2} & E^s_{\beta,1} \end{pmatrix} \begin{pmatrix} \hat{x}\cdot\hat{\beta} & \hat{y}\cdot\hat{\beta} \\ -\hat{y}\cdot\hat{\beta} & \hat{x}\cdot\hat{\beta} \end{pmatrix}, \tag{3.6}$$

where f is a factor for energy conservation, which can be determined from the normalization of the phase function. It is evident from Eqs. (3.4)–(3.6) that the scattered fields associated with the incident polarization configurations $(E^i_x, E^i_y) = (1,0)$ and $(0,1)$ are required to solve the scattering matrix. In the deterministic algorithm (Cai and Liou, 1982), the scattered fields corresponding to these two incident polarization configurations can be simultaneously solved in the ray-tracing calculation by performing a number of coordinate transformations. However, separate ray-tracing calculations are required for the x- and y-polarized incident configuration in the Monte Carlo/ray-tracing method. This is because the ray paths determined by a stochastic procedure may differ for two rays with non-identical incident polarization configurations even if they impinge on a same point at the particle surface. For example, a ray with the x-polarized incidence may escape the scatterer after two internal reflections whereas one with the y-polarized incidence may undergo three internal reflections. Physically, these non-identical ray-paths in the two cases are caused by the different ratios of the two polarized field components with respect to the incident plane on particle surface. That is, the reflection criterion differs in these two cases. In light of the preceding discussions, the stochastic approach is not as efficient as the deterministic algorithm because separate ray-tracing calculations are required by the former for the two incident polarization configurations. However, it is extremely difficult for the latter method to be applied to complex ice crystals due to a significant number of sub-rays involved. It should be noted that the separate computations for the two polarized incidences are usually required for a number of accurate numerical methods such as the finite-difference time-domain (FDTD) technique (Umashankar and Taflove, 1982; Yang and Liou, 1995,1996a) and the digitized Green's function algorithm (Goedecke and O'Brien, 1988).

If the field components perpendicular and parallel to the incident plane at a point on particle surface are E_r and E_l for a given incident polarization configuration, say, $(E^i_x, E^i_y) = (0,1)$, the reflection criterion for stochastic simulations of ray-propagation can be obtained precisely as follows:

$$r = \frac{|R_l|^2 |E_l|^2 + |R_r|^2 |E_r|^2}{|E_l|^2 + |E_r|^2}. \tag{3.7}$$

In numerical computations, if a random number distributed uniformly in the region of (0,1) is larger than the criterion, refraction is expected; otherwise, reflection occurs. If reflection happens, the two components of the reflected field (E^r_l and E^r_r) are given by

$$\begin{pmatrix} E^r_l \\ E^r_r \end{pmatrix} = \begin{pmatrix} R_l & 0 \\ 0 & R_r \end{pmatrix} \begin{pmatrix} E_l \\ E_r \end{pmatrix}. \tag{3.8}$$

A similar expression can be obtained for the transmitted field. When a ray finally escapes from crystals, the contribution of this ray to the phase matrix, which can be obtained by using Eq. (3.6), should be normalized according to the energy carried by the corresponding initial incident ray in the Monte Carlo/ray-tracing calculation. In this manner, the polarization configuration can be accounted for properly. To economize the computation effort and to circumvent the repeating ray-tracing calculations for the two incident polarization configurations, ray-paths can be selected to be the same for the two rays that have different initial polarization configurations but impinge on an identical point on the particle surface. In this case, the reflection criterion given by Eq. (3.7) should be modified as follows:

$$r \approx \frac{<R^2E^2>}{<E^2>}, \tag{3.9}$$

where

$$<R^2E^2> = |R_l|^2 (|E_{l,1}|^2 + |E_{l,2}|^2)$$

$$+ |R_r|^2 (|E_{r,1}|^2 + |E_{r,2}|^2), \tag{3.10}$$

$$<E^2> = |E_{l,1}|^2 + |E_{l,2}|^2$$

$$+ |E_{r,1}|^2 + |E_{r,2}|^2. \tag{3.11}$$

In Eqs. (3.10) and (3.11), the subscripts 1 and 2 indicate the x- and y-polarized incidence, respectively. When reflection or refraction occurs, the field amplitude can be obtained by equations similar to Eq. (3.8) for the two incident polarization configurations. Although Eq. (3.9) is an approximate criterion for ray reflection, we have found that the effect of the inaccuracy associated with this approximation on the phase matrix is negligible.

When absorption is involved, Takano and Liou (1995) have used the standard hit-and-miss Monte Carlo procedure (Lux and Koblinger, 1991) to account for the absorption of ice crystals. The path-length within which a ray is absorbed is determined randomly by a random number, ζ, as follows:

$$l_a = -\ln(\zeta/2km_i), \tag{3.12}$$

where k is the wavenumber of the incident wave, and m_i is the imaginary part of the ice refractive index. A ray is absorbed if the distance between two successive internal reflection points for this ray is larger than the absorption path-length. In this study, we use a more computationally efficient approach to account for the absorption of ice crystals. When an incident ray is released, an initial weighting parameter, w, which is proportional to the ray cross section or the energy carried by the ray, is assigned to the ray. When this ray is refracted into the particle and propagates a distance of d inside the particle, the weighting parameter is decreased by

$$w' = w\exp(-i2km_id). \tag{3.13}$$

When this ray finally escapes from the ice crystal in the ray-tracing computation, the contribution of the ray to the phase matrix is normalized with respect to the final weighting parameter. In this manner, a number of stochastic tests involving the generation of random numbers can be avoided in determining whether a ray is absorbed. For the ray-tracing computation involving complex ice crystal shapes, it is critical to determine the incident point on the particle surface correctly. An efficient approach has been applied in the present study. First, an incident ray can be specified by its incident direction and a point on an envisioned surface which just encloses the particle. The spatial point where the ray intersects with the envisioned surface is randomly selected on the basis of the procedure suggested by Wendling et al. (1979). Once the incident ray is determined, we can further determine whether the ray intersects with the ice crystal. If it does, the ray will be traced until it leaves the ice crystal under the condition that re-entry does not occur; otherwise, another ray is sampled. In the present numerical computation, a coordinate-independent ray-tracing scheme in vector form (Yang and Liou, 1996b) is employed to calculate the directions of rays and the polarized fields associated with the rays.

The diffracted field produced by complex crystals is solved approximately on the basis of the diffraction associated with a hexagon, under the condition that the two shapes lead to the same projected-area on a screen perpendicular to the incident direction. In the previous GO method, a scalar diffraction formulation has been used. To include the polarization in the diffraction calculation, we have developed an improved formulation presented in Appendix. The addition of the diffracted and Fresnelian rays is based on the method developed by Takano and Liou (1989a) in which the effect of the delta-transmission is accounted for.

The conventional ray-tracing technique employed in the previous studies requires a large size parameter for the localization of geometric rays. This method breaks down in terms of inaccuracy when the size parameters are on the order of 50 and 100 for simple particle geometries such as spheroids, and circular and hexagonal cylinders (Macke et al., 1995; Wielaard et al., 1997; Yang and Liou, 1995), depending on whether the extinction and scattering cross sections or the phase matrix are computed, respectively. For complex ice crystal shapes such as aggregates and particles with rough surface, a quantitative criterion about the applicability of the ray-tracing technique with regard to the characteristic dimensions of the smallest particle elements and the rough surface undulations is still avoid at this point, which is a topic deserves a further study. To solve for the scattering properties of ice crystals with moderate size parameters, improvements have been made to circumvent the shortcomings of the conventional ray-tracing technique (Muinonen, 1989; Yang and Liou, 1996b, 1997). In particular, the ray-by-ray integration algorithm developed by Yang and Liou (1997) has been proven to be a generalization of the anomalous diffraction theory (van de Hulst, 1957) that is applied to the calculation of the extinction and absorption cross sections for optically tenuous particles. For a scattering problem involving nonspherical ice crystals with small size parameters, the discrete dipole approximation method (Purcell and Pennypacker, 1973; Flatau et al., 1990) and the FDTD technique (Yang and Liou, 1995, 1996a) can be applied, which, however, can only be applied for the size parameters smaller than on the order of 10 in practice because of their tremendous demand on computer CPU time and memory. It should been pointed out that exact solutions have been obtained for spheroids and circular cylinders with size parameters larger than 100 by using the T-matrix technique (Mishchenko, 1993; Wielaard et al., 1997) and the full wave method (Zuffada and Crisp, 1997). In the present study, we have applied the improved ray-tracing technique to transform the near-field obtained by ray-optics to far-field (Yang and Liou, 1996b) in the computation of the phase matrix when the size

parameter is smaller than 100. In addition, the ray-by-ray integration technique (Yang and Liou, 1997) has been employed to calculate the extinction and absorption cross sections.

4 Numerical Results and Discussions

According to replicator and two-dimensional optical cloud probe (2D-C) data, the sizes of ice crystals with complex shapes are normally large while a major portion of small ice crystals have simple geometries (e.g., Mitchell and Arnott, 1994). Large ice crystals tend to be oriented with their maximum cross sections facing the upwelling air in the atmosphere, because of their large Reynolds number. Under such orientations, the phase matrix depends not only on the scattering zenith angle, but also on the azimuthal angle of the scattering plane. For simplicity, we assume random orientations for the ice crystals in the present study. Random orientations of ice crystals can be expected in a turbulent atmosphere. In the present computations, the contributions of 10^6 outgoing rays have been accounted for in the calculation of the phase matrix while total incident rays sampled randomly on the envisioned surface defined in Section 3 may be much more than 10^6, depending on a specific ice crystal geometry. The improved Monte Carlo/ray-tracing method has been validated by comparison with the deterministic ray-tracing algorithm for the light scattering by solid hexagonal ice crystals. The differences between the phase matrix computed by the two methods are less than 0.1%.

Figure 4 shows the phase function and the degree of linear polarization (DLP) for fernlike crystals and ice plates with dendritic extensions for wavelength 0.55 μm. The absorption of ice at this wavelength is essentially negligible. The shapes of these ice crystal cross sections are also shown in the diagram. The phase function and the DLP values for the equivalent hexagonal plates that have the same projected-area as the complex crystals are also presented for comparison. The lengths of fernlike sub-branches in cases 1 and 3 vary randomly whereas the fernlike structures in cases 2 and 4 are determined by the enveloping contours discussed in Section 2. A general feature of the phase function for these complex crystals is the disappearance of the 22° scattering peak. This is because the fernlike extensions do not produce the minimum deviation of 22° for ray transmission. The 46° halo peak caused by the ray transmission associated with side-and-end prisms, however, is almost the same for the complex and the equivalent crystals. From Figure 4, it is evident that substantially more energy is scattered in the angular region $1° - 20°$ by the complex crystals than the equivalent hexagonal plates. In addition, the lateral and backward scattering are also larger in the cases of complex crystal geometries. This is in agreement with the study by Zerull et al. (1980) who noted that the scattering patterns of irregularly shaped particles differ significantly from those of simple geometry particles, as irregular particles scatter more energy into the lateral direction. The phase function values associated with the equivalent hexagonal ice crystals are larger than those associated with the corresponding complex shapes in the angular region from 0° to ~ 1°. Because the complex ice crystals and their equivalent hexagonal ice crystals possess the same projected areas, the larger forward scattering associated with the latter is caused by Fresnelian rays. Physically, the probability that a ray transmits through the particles without a (or with a slight) deviation from the incident direction is larger for hexagonal shape because of the parallel faces involved. The magnitudes of the DLP variations versus scattering angle for the complex crystal are much smaller than those for the equivalent hexagons. In particular, the intensive, negative polarization associated with the backward scattering, which is observed in the case of hexagonal ice crystal, is reduced significantly by the fernlike extensions. It has been reported by Santer et al. (1985) that the observed DLP values for Martian white clouds are close to zero at backscattering angles. However, theoretical results using solid hexagonal columns and plates show significantly large negative polarization (Takano and Liou, 1989a,b). Thus, it seems necessary to incorporate the polarization properties of the ice crystals with shapes more complex than regular hexagons for a proper interpretation of the observed DLP values.

Presented in Figure 5 are the phase function and the other non-zero elements of the phase matrix normalized by P_{11} for the ice plates with dendritic extensions at the near-infrared wavelength 2.2 μm. Note that the absorption of ice at this wavelength cannot be neglected. Similar to the case of the visible wavelength, at the near infrared wavelength the complex ice crystals scatter more energy for the scattering angles larger than about 2° whereas the forward scattering around 0° is larger in the case of equivalent hexagons. The halo peak at 19° cannot be observed for the dendritic crystals because the fernlike extensions largely block the ray transmissions associated with side-to-side prisms, which undergo the

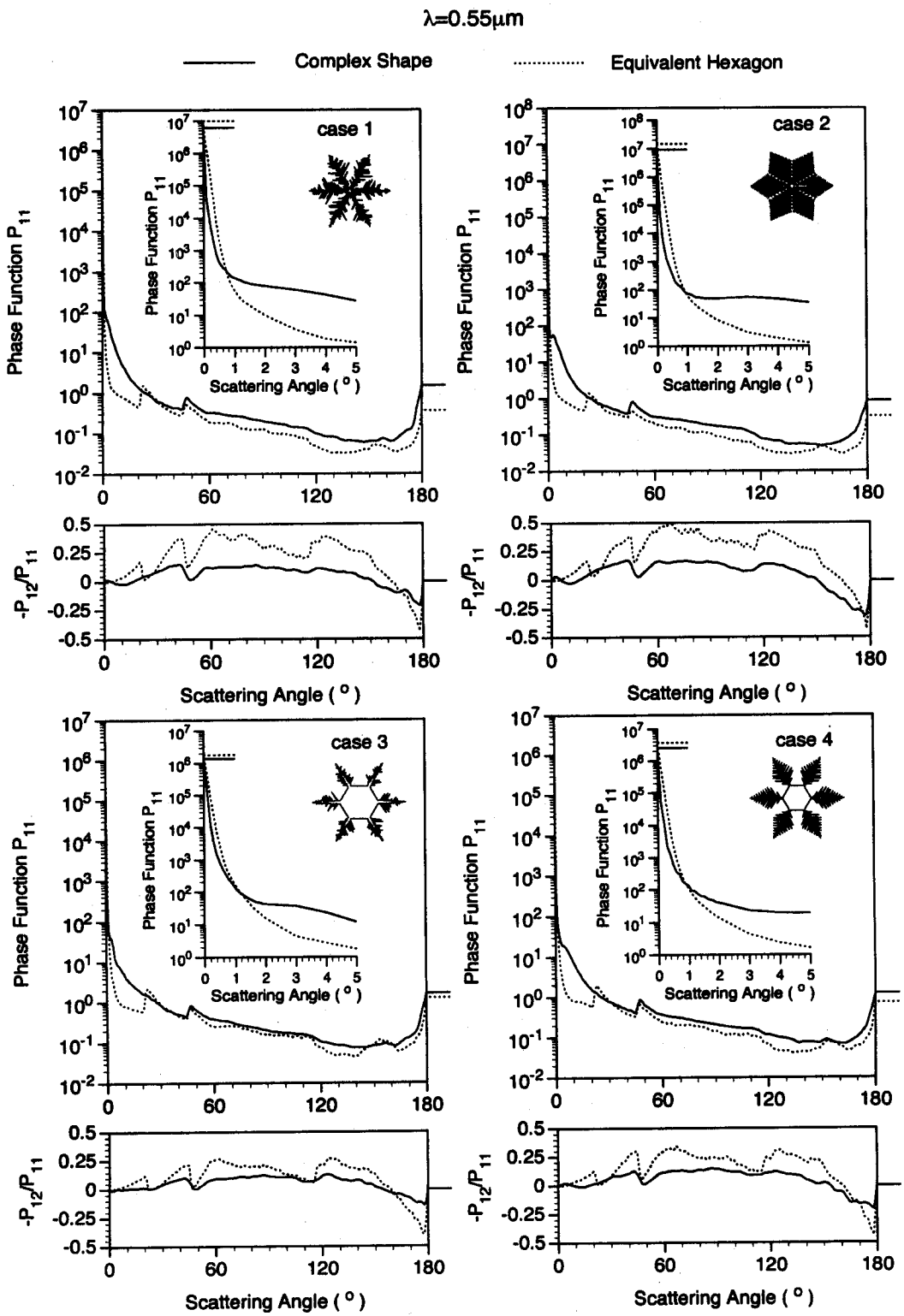

Figure 4: Phase function and the degree of linear polarization for the fernlike and dendritic crystals at 0.55 μm. The parameters defined in Figure 1a for determining the ice crystal dimensions, (γ, η, ξ, N, ρ, a_1, a_2, L), are (30°, 30°, 35°, 20, 0.5, 20 μm, 600 μm, 50 μm), (30°, 30°, 35°, 10, 0.556, 20 μm, 600 μm, 50 μm), (5°, 30°, 35°, 10, 0.5, 100 μm, 150 μm, 50 μm), and (3°, 40°, 30°, 10, 0.5, 100 μm, 240 μm, 50 μm) for cases 1–4, respectively. L denotes ice crystal thickness. Also shown are the results for the equivalent hexagonal plates.

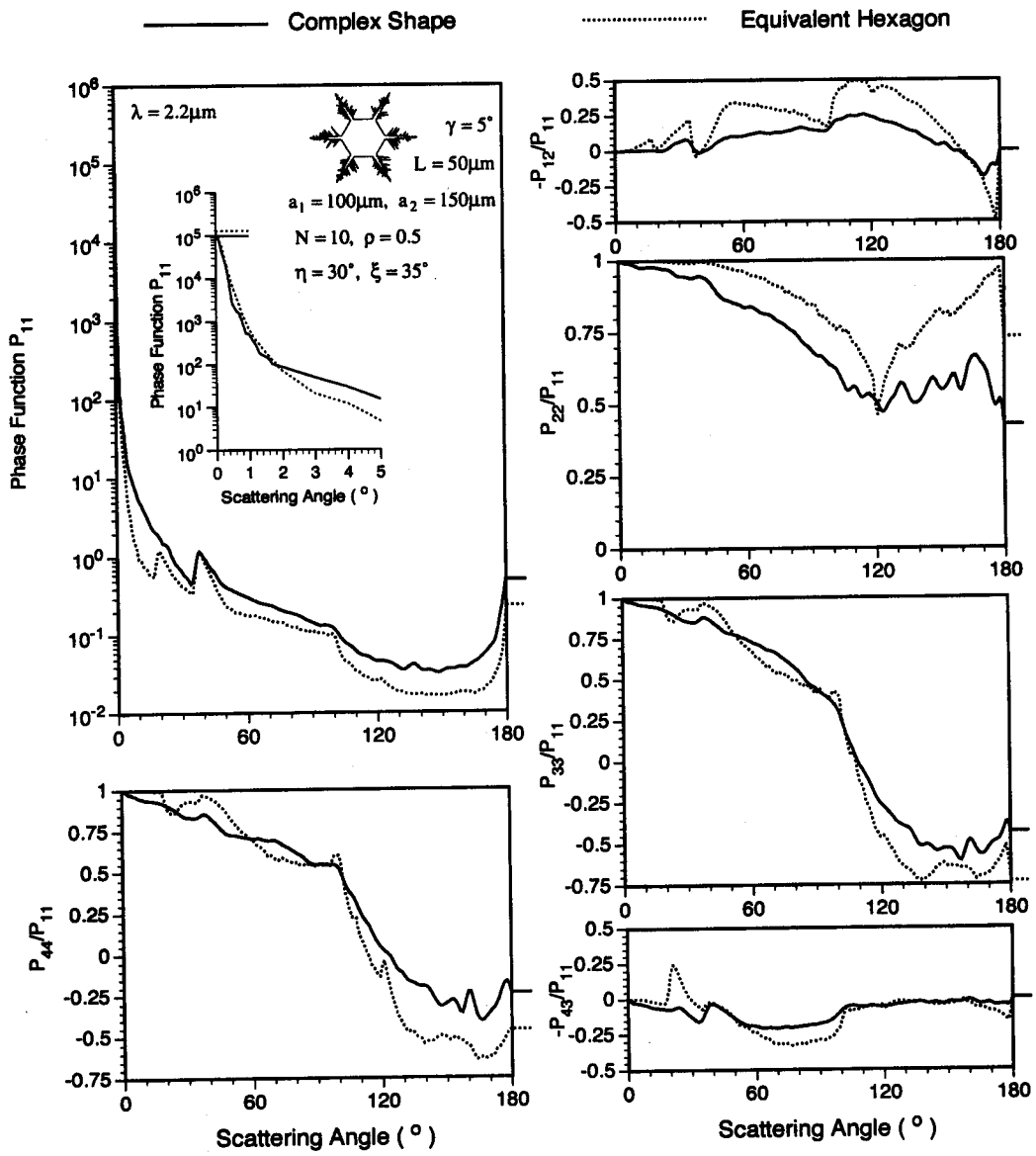

Figure 5: Complete non-zero elements of phase matrix for dendritic crystals at 2.2 μm.

19° minimum deviation. For both the phase function and the DLP values, it can be seen that the differences between the results for the complex and equivalent hexagonal ice crystals are more significant when absorption is involved, as evident from the comparison of Figure 5 with case 3 in Figure 4. The values of $-P_{43}/P_{11}$ are very close for the two crystal geometries with the exception of a 19° peak observed for the equivalent hexagonal case, which corresponds to the halo peak in the phase function. The variations of P_{33}/P_{11} and P_{44}/P_{11} as the functions of scattering angle are very similar for the simple and complex crystal geometries, although the values of P_{33}/P_{11} and P_{44}/P_{11} are much smaller for the scattering angles larger than 100° for the complex crystals. From the comparisons of the polarization elements of the phase matrix for the dendritic and equivalent crystals, the most significant difference are noted for P_{22}/P_{11}, in particular, in the angular region around backscattering direction. Because substantial differences exist in the single-scattering phase matrix for complex and hexagonal crystals, it is anticipated that the polarization pattern of light beams produced by multiple scattering inside cirrus clouds cannot be solved properly by using the equivalent hexagonal approximation if a substantial number of complex ice crystals exist.

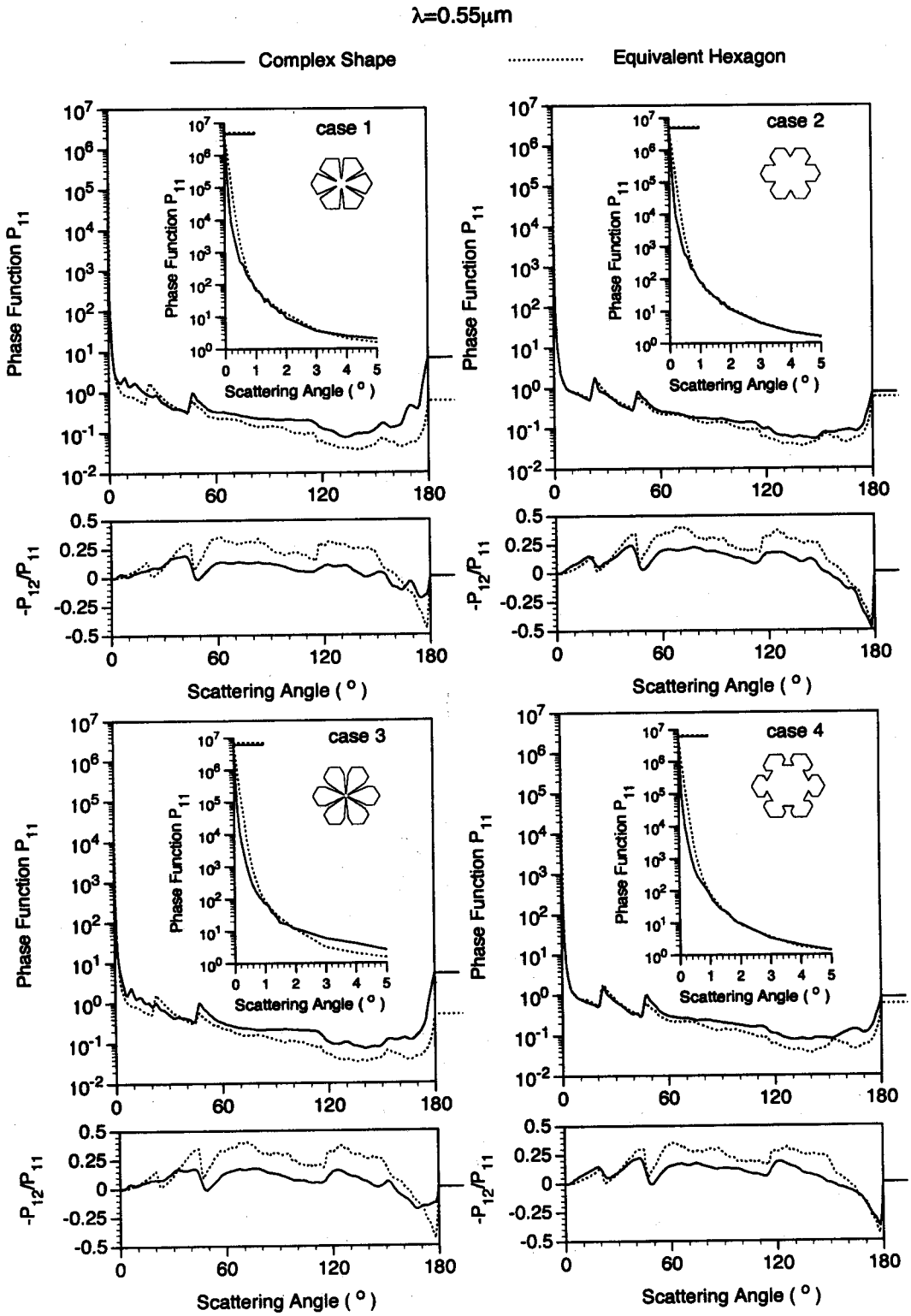

Figure 6: Phase function and the degree of linear polarization for the plates with broad and sectorlike branches at 0.55 μm. The parameters defined in Figure 1b for determining the particle dimensions are ($\beta = 25°$, $a_1 = 50$ μm, $a_2 = 250$ μm, $L = 50$ μm), ($\beta = 30°$, $a_1 = 150$ μm, $a_2 = 150$ μm, $L = 50$ μm), ($\beta = 25°$, $a_1 = 20$ μm, $a_2 = 200$ μm, $a_3 = 80$ μm, $L = 50$ μm), and ($a_1 = 200$ μm, $a_2 = 120$ μm, $a_3 = 60$ μm, $h/a_2 = \sqrt{3}/4$, $L = 50$ μm) for cases 1–4, respectively. L denotes ice crystal thickness.

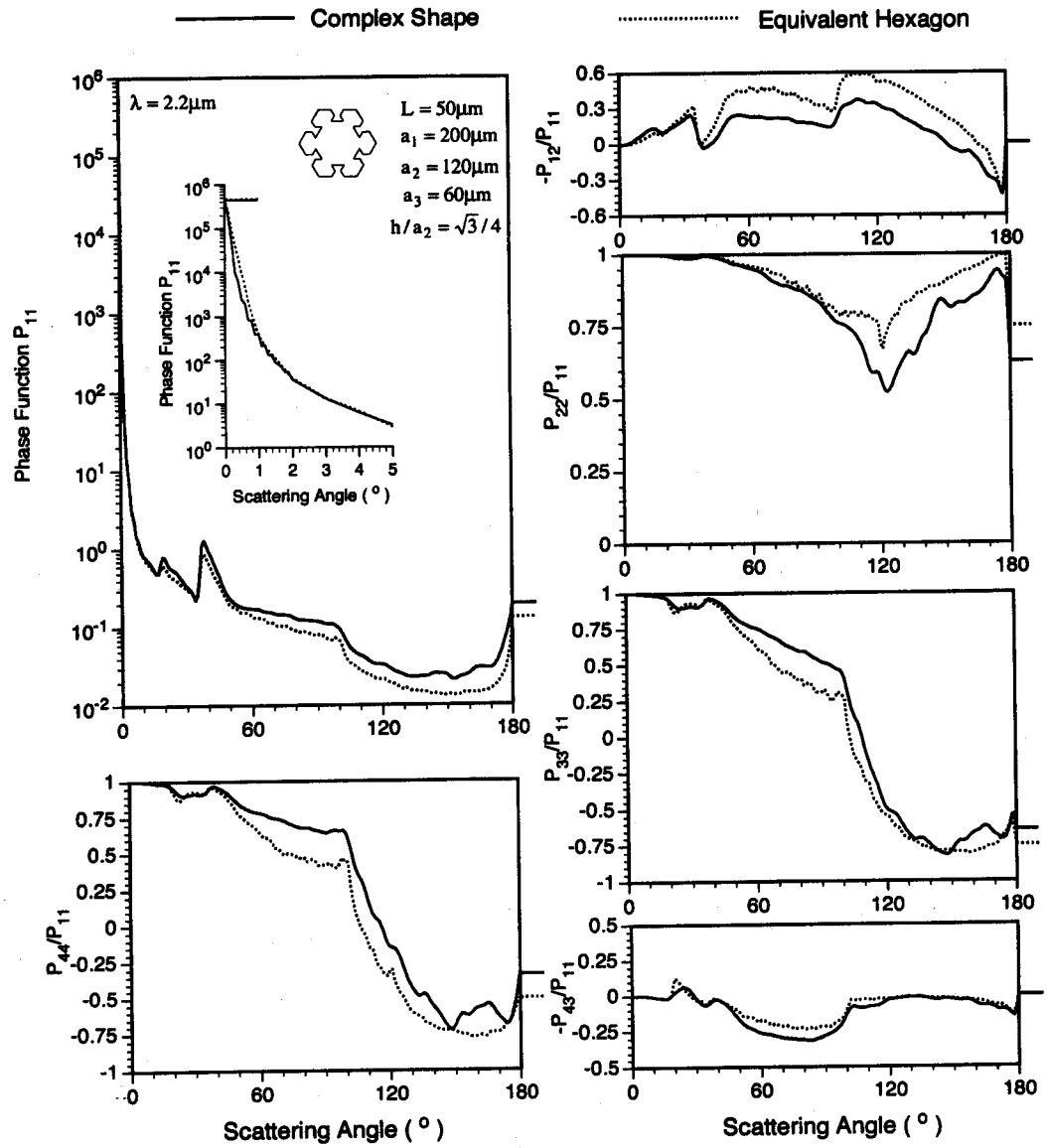

Figure 7: Complete non-zero elements of phase matrix for crystals with broad branches at 2.2 μm.

Figure 6 is similar to Figure 4, except that the complex crystal geometries in the present diagram are plates in sectorlike form and plates with sprouts and broad branches. In cases 1 and 3, where the complex ice crystals are in sectorlike form, the 22° halo peak disappears as a result of the complex crystal geometry; however, some small fluctuations can be noted in the angular region 2° – 20°. These small fluctuations are caused by the multiple reflections and transmissions of rays between the sectorlike branches of crystals. For the crystals in sectorlike form, we also note the considerably large differences of the P_{11} and the DLP values in the comparison of the results for the complex and their equivalent hexagonal crystals. The differences are more pronounced for scattering angles around 180°. For cases 2 and 4, where the crystals have broad branches and sprouts, the variation tendencies of the phase function and the DLP values are very similar for the complex geometries and the equivalent hexagons. This is because the crystal cross sections of these complex crystals retain the major characters of hexagonal structure for the ray-tracing calculation. Thus, a significant 22° halo peak and intensive, negative backward scattering polarization can be observed for the two crystal geometries. In addition, the energies scattered into the angular re-

gion of 2° – 20° are almost the same for the complex and equivalent hexagonal crystals. However, it should be noted that the crystals with sprouts and broad branches scatter more energy in the lateral and backward directions than their equivalent counterparts, even though the preceding similarities are observed.

Figure 7 shows the complete nonzero elements of the phase matrix for the ice plates with six hexagonal sprouts at the near-infrared wavelength 2.2 μm. From a comparison of the phase function and the DLP values in the cases of the visible and the near-infrared wavelength, it can be noted that the differences of the results for complex and equivalent hexagonal crystals are larger when absorption is concerned. This is because the equivalent crystals have a large absorption due to a longer mean length for ray-paths inside the particles. For $-P_{43}/P_{11}$, P_{33}/P_{11} and P_{44}/P_{11}, similarities can be noted for the two kinds of crystal geometries. In particular, a very good agreement is observed for $-P_{43}/P_{11}$. The differences for P_{22}/P_{11} are noted mainly for the scattering angles larger than 90°.

Figure 8 shows the phase function and DLP for two kinds of fractal crystals, the Koch-islands and hexagonal aggregations, at both visible and near-infrared wavelengths. The results for the equivalent hexagonal counterparts are also shown. The phase function of the Koch-islands at a visible wavelength in the 2-D case has been computed by Macke and Tzschichholz (1992), who found that there are six basic significant scattering peaks. However, the idealized 2-D case is a situation for which the incident rays are perpendicular to the c-axes of the crystals. When various orientations of the crystals are accounted for in averaging the phase function, many scattering peaks observed in the 2-D case (e.g., a pronounced peak at 120°) do not appear in the 3-D case. At the visible wavelength of 0.55 μm, it is evident that the overall scattering feature of the Koch-island is very similar to its equivalent hexagonal counterpart; however, the lateral scattering and backscattering are larger, and the magnitude of polarization is smaller for the Koch-island. When absorption is involved at 2.2 μm, it can be noted that there are two peaks at 19° and 37° in the phase function of the Koch-islands, whereas there is only one peak at 37° in the equivalent hexagonal ice crystal. This is because the mean length for ray propagation inside ice crystals is longer for hexagon than for the Koch-island. Thus, the rays undergoing two refractions associated with side-to-side prisms, which produce the 19° halo peak, are largely absorbed inside the solid crystals. In addition, it is evident that the differences between results for the Koch-island and equivalent hexagonal increase when absorption is involved. For the phase function and DLP for the hexagonal fractal aggregations, the difference of scattering by the crystals and their equivalent hexagonal counterparts is similar to the case of the Koch-islands. However, it should be noted that the increase of the lateral and backward scattering by the complex crystal is more significant in the case of fractal aggregations.

Figure 9 shows the complete nonzero elements of Stokes scattering phase matrix of ice crystal aggregates for three roughness conditions. The geometric sizes of aggregates are characterized by their maximum dimensions, which are selected as 200 μm for the results presented in this diagram. In the numerical computation, the number of the hexagonal elements of which an aggregate consists is randomly selected from 2 to 8 in the procedure of averaging the effect of aggregate orientations. The selected hexagonal elements are attached together without overlap by properly selecting their geometric dimensions. The sizes of these elements are then scaled so that the maximum dimension of the aggregate is 200 μm.

It is evident from Figure 9 that the surface roughness condition largely affects the scattering properties of ice crystals. For smooth case (σ=0.0), the pronounced peaks at 22° and 46° and the scattering maximum at 154° are obvious for the computed phase function. For a moderately roughness condition (σ=0.03), the 46° scattering peak and the 154° scattering maximum are smoothed out in the phase function although a broad scattering maximum 22° is still noticeable. In addition, the backscattering is substantially reduced by the effect of surface roughness. When a substantial roughness condition (σ=0.1) is imposed in the single-scattering calculation, the computed phase function is essentially featureless. Physically, the surface roughness of ice crystals causes the spreading of the collimatic light beams that are associated with the 22° and 46° minimum deviations of refraction. Rough surface also leads to the spreading of the rays that emerge in the directions around 154° and the backscattering after an internal reflection.

The effect of the surface roughness on polarization configuration is more significant for P_{12}/P_{11}, P_{22}/P_{11}, P_{33}/P_{11} than for P_{44}/P_{11} and P_{43}/P_{11}. In particular, the degree of linear polarization given by $-P_{12}/P_{11}$ is substantially reduced by the roughness effect.

Shown in Figure 10 are the nonzero elements of the phase matrix for various ice crystals with a very deep roughness condition. The aggregate geometry in Figure 10 is the same as in Figure 9. The dimension of

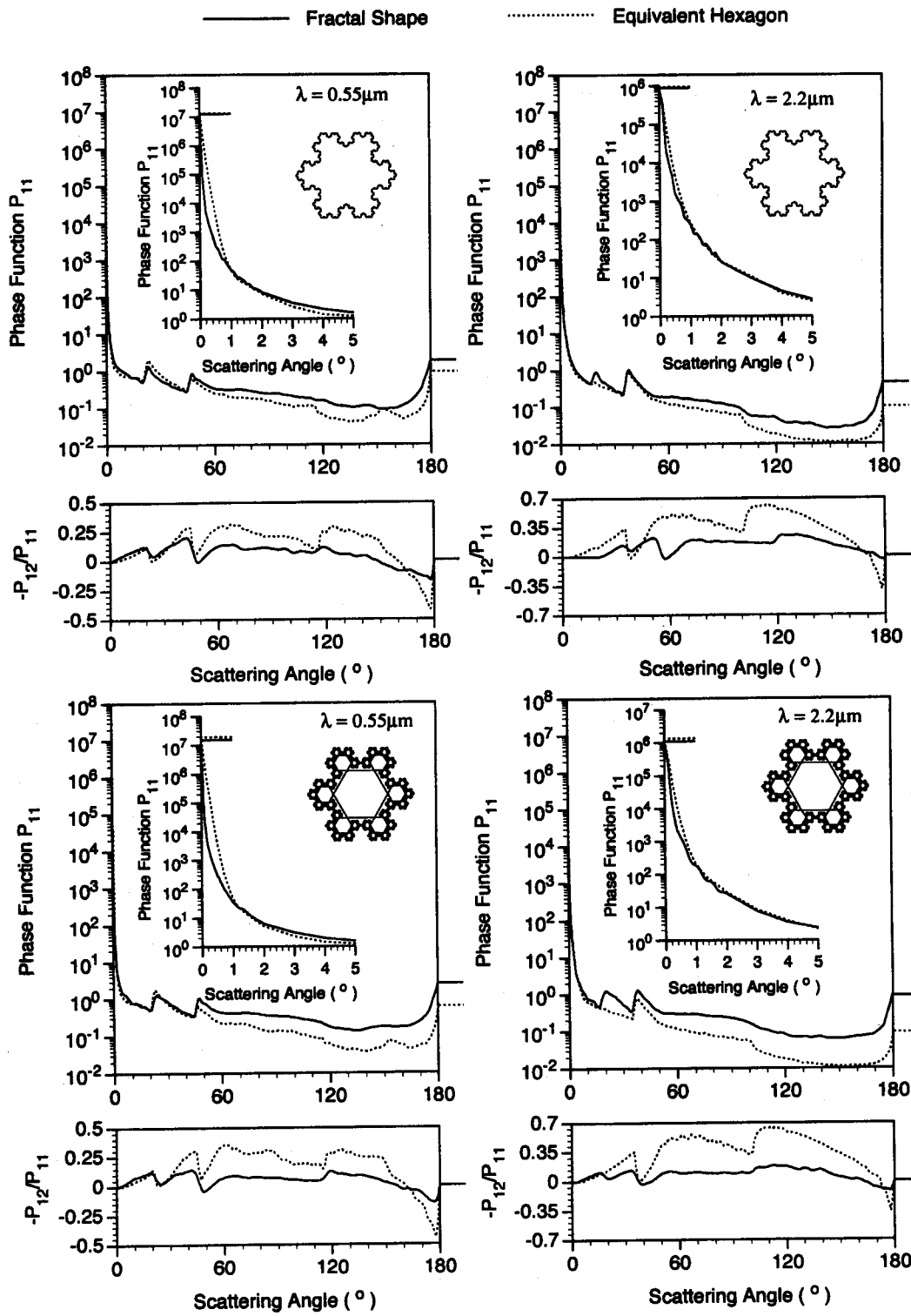

Figure 8: The phase function and the degree of linear polarization for fractal crystals at 0.55 μm and 2.2 μm. The parameters defining the particle dimensions are ($a = 500$ μm, $L = 100$ μm) and ($a_1 = 310$ μm, $a_2 = 100$ μm, $a_3 = 35$ μm, $a_4 = 10$ μm, $a_5 = 5$ μm, $L = 100$ μm) for the Koch-island and the fractal aggregation, respectively. L denotes ice crystal thickness.

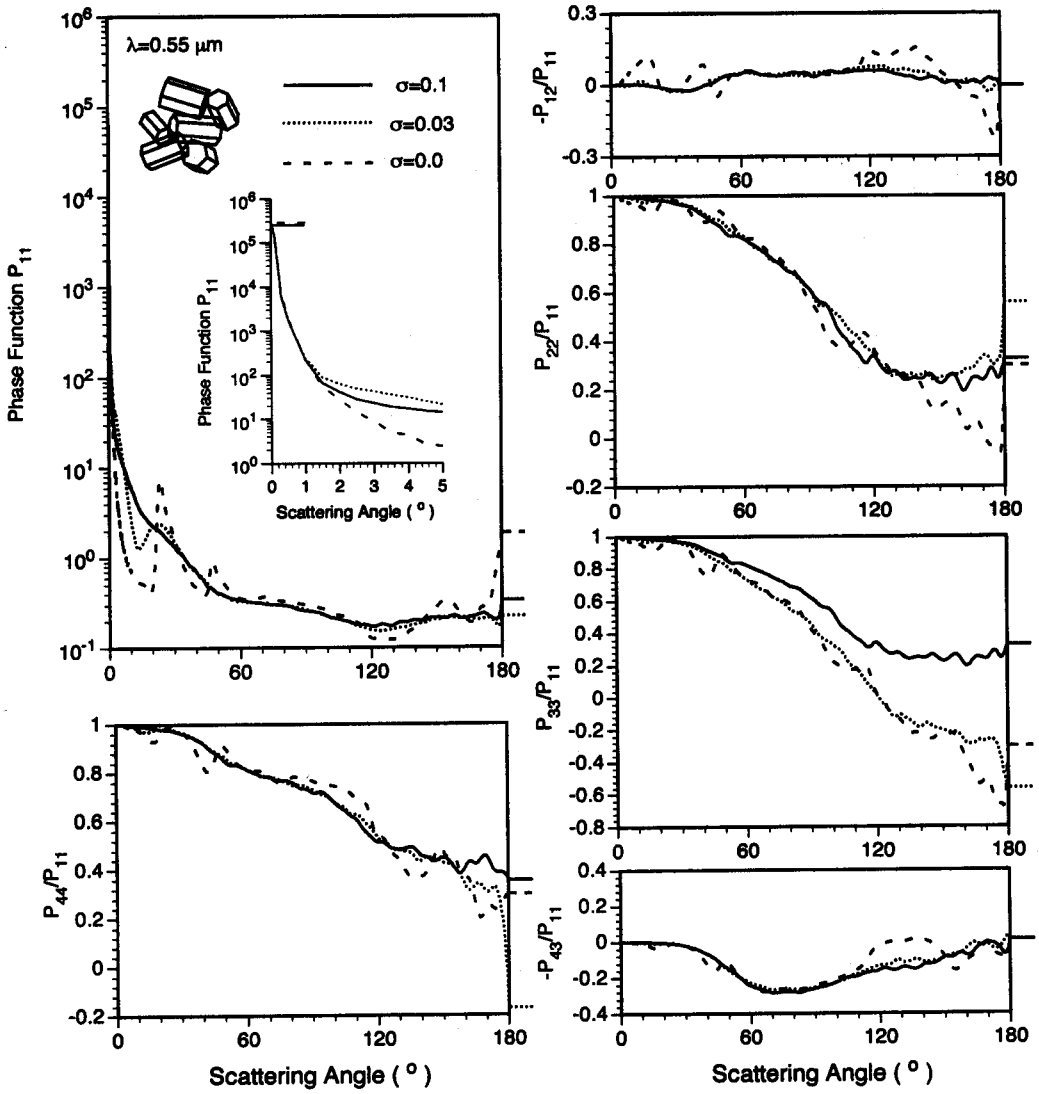

Figure 9: The nonzero elements of phase matrix of aggregates for three roughness conditions corresponding to smooth, moderate,and deep roughness, respectively.

the plate is $a/L = 100/50$ μm. The size of the hollow column is $a/L = 50/200$ μm. The depths of the hollow structures at both ends are randomly selected from 0 to 100 μm. To define the bullet rosette, we use $L/a = 90/50$ μm for the columnar parts of individual bullet elements. The pyramidal tips of the bullet elements can be specified by the semi-widths of the columnar parts and the inclination angle of pyramidal faces with respect to the major axes of the bullet elements. Following Greenler (1980), we select 28° for this inclination angle in the present calculation. It can be noted that the maximum sizes of these four shapes are approximately the same.

The shape effect of ice crystals is insignificant when the particle surface is very rough. In particular, the computed polarization configurations for the four geometries are almost the same although these particle shapes are quite different, as is evident from Figure 10. Convergence of the phase function part contributed by Fresnelian rays is noted for plates and hollow columns, and for bullet rosettes and aggregates. That is, two converged results for the phase function part associated with Fresnelian rays can be obtained for ice crystals with multi-elements and for those with a single element, respectively. Nevertheless, the differences are not substantial in terms of

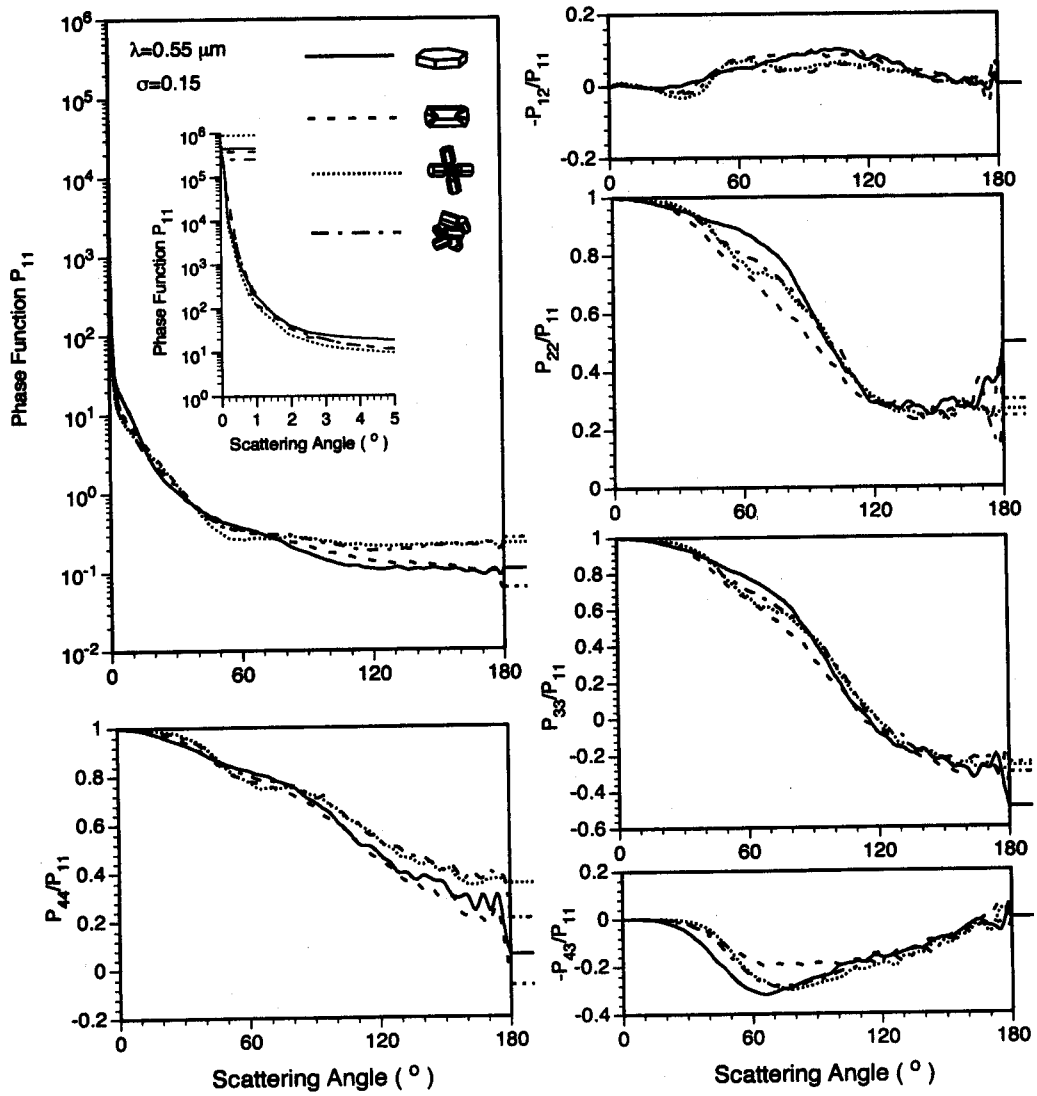

Figure 10: Comparison of phase matrix for plates, hollow columns, bullet rosettes, and aggregates for a substantial roughness condition.

scattered energy for the two converged values of the phase function part contributed by Fresnelian rays. Thus, the angular scattering pattern and the polarization configuration associated with Fresnelian rays for a simple ice crystal geometry can be used to represent those for complex ice crystal geometries if a substantial roughness condition is imposed.

Displayed in Figure 11 are various kinds of ice crystal shapes along with their phase function patterns at 0.63 μm wavelength for large size parameters (> 200). Surface roughness is not imposed for these phase function calculations. The parameters defining the geometric sizes of these ice crystals are not presented in the diagram for the sake of a concise illustration. It should be pointed out that the phase function pattern for a nonabsorptive wavelength in the lateral and backward directions is independent of particle size if the particle is large. The particle size only affects the magnitude of forward diffraction peak. Similar scattering characteristics can be seen for solid column and plate, double plates, plate with attachments, and aggregate, because these shapes are composed of a single hexagon or multiple hexagonal elements. Similarity is also observed in the results for bullet rosettes with 4 and 6 branches. However, sub-

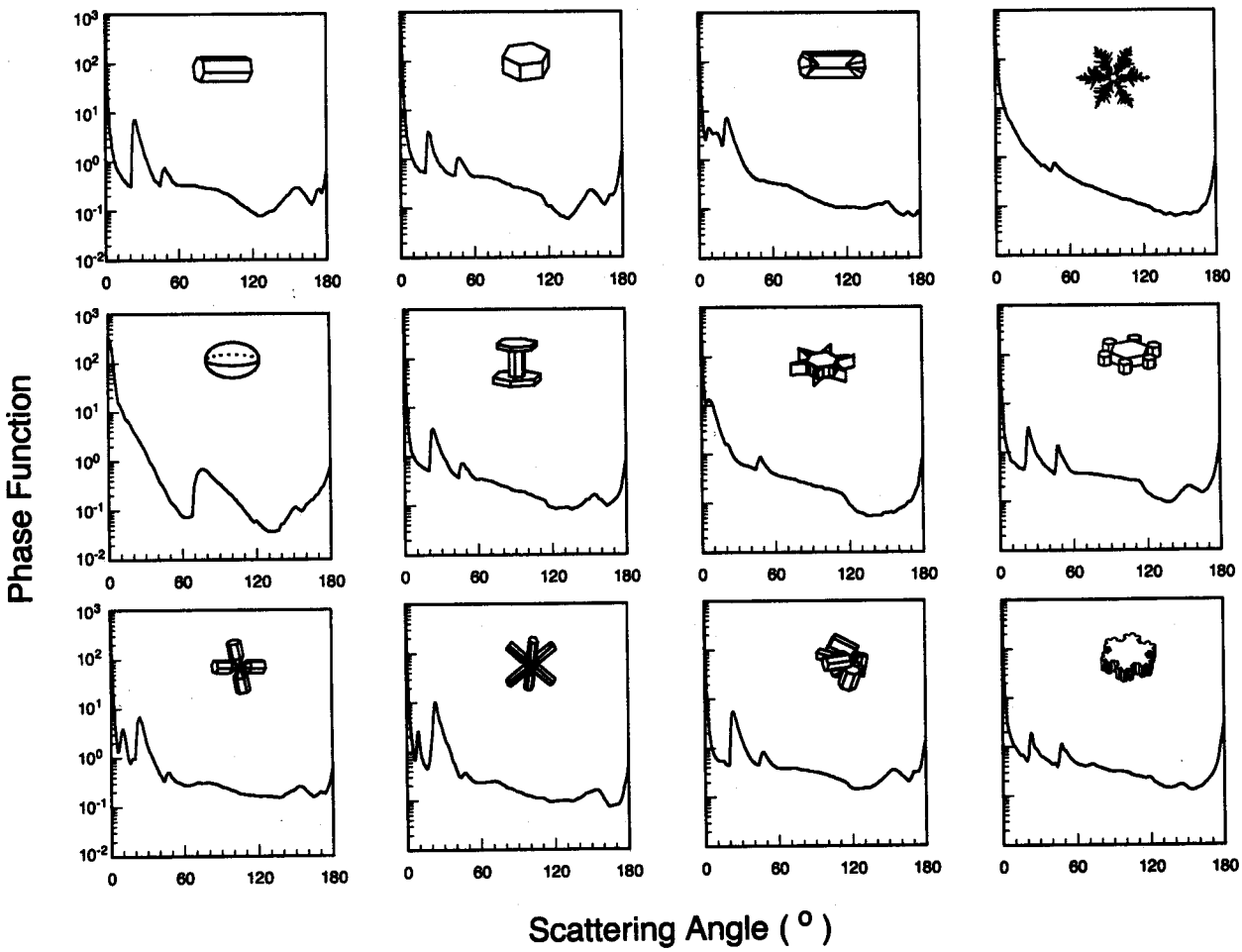

Figure 11: Comparison of phase function for various ice crystal shapes at 0.63 μm wavelength.

stantial differences are evident in the comparison of the phase functions associated with hollow column, spheroid, bullet rosettes, fern-like plate, and dendrite. In particular, fern-like extensions largely smooth out the scattering peaks corresponding to halos. According to Figure 11, it is evident that the basic structures of complex ice crystals are critical to the determination of the angular scattering patterns of these ice crystals.

The single-scattering parameters important to the calculation of the radiative transfer in the atmosphere are the extinction coefficient, single-scattering albedo, and the phase function. For the two-stream and four-stream radiative transfer schemes used in climate modeling, the asymmetry factor other than the detailed angular variation pattern of phase function is sufficient. Note that the first four Legendre expansion coefficients of the phase function, which are required by the four-stream radiative transfer scheme, can be determined approximately by using the asymmetry factor if the strong forward diffraction peak is removed from the phase function (Fu and Liou, 1993). Parameterization of the preceding single-scattering quantities in terms of mean effective size for a given size distribution of ice crystals and ice water content (IWC) has been conducted on the basis of the ray-tracing results (e.g., Ebert and Curry, 1992; Fu and Liou, 1993; Fu, 1996). In order to include the effect of complex ice crystals in future parameterization, we have established a database of the fundamental scattering and absorption parameters for various ice crystal shapes and sizes for solar spectrum. The development of a database for infrared wavelengths is currently ongoing by using a combination of the FDTD technique and the improved geometric optics method.

In the present database for solar wavelengths, the spectral region from 0.2 to 5 μm is divided into 56 narrow bands. For each band, the refractive index

of ice complied by Warren (1984) with a modification based on recent measurements (Gosse et al., 1995) is used, which is further weighted by using the detailed solar irradiance data from LOWTRAN7 (Kneizys et al., 1988) in the present calculation. The single-scattering parameters for various ice crystal shapes are computed at the band centers for 23 bins of ice crystal sizes: 5–10, 10–20, 20–30, 30–40, 40–50, 50–70, 70–90, 90–110, 110–150, 150–200, 200–250, 250–300, 300–400, 400–500, 500–600, 600–700, 700–800, 800–1000, 1000–1300, 1300–1500, 1500–2000, 2000–3000, and 3000–4000 μm. These bins are defined with respect to the maximum dimensions of ice crystals. The aspect ratios for ice crystal geometries used in the present study are based on those reported by Auer and Veal (1970) and Mitchell and Arnott (1994). After the database is established, it is straightforward to obtain the single-scattering properties of ice crystals for a given size distribution and the corresponding percentage of various ice crystal habits.

To illustrate the effect of crystal shape on the single-scattering properties for a given size distribution, we have selected two cases corresponding to a cold and a warm cirrus, for which small and large ice crystals are predominant, respectively. The *in situ* observed size distribution of cold cirrus shown in Figure 12 was obtained during an experiment sponsored by the U.S. Department of Energy that was carried out over the Cloud and Radiation Testbed (CART) site located in northern Oklahoma and southern Kansas on April 19, 1994. The data were derived near the top (z=13.4 km, T=−69.4°C) of an optically thin cirrostratus cloud (Sassen, personal communication). The size distribution data were derived from the FSSP device, which has been shown to yield reliable data when ice crystals with sizes larger than 50–100 μm are absent (Gayet et al., 1996). As demonstrated in Figure 12, the calculated extinction coefficients of the cold cirrus are significantly different for these five shapes (Note that effect of surface roughness is not noticeable for the extinction coefficients). In particular, the results associated with columns and hollow columns are larger than those associated with aggregates by about a factor of 2. When the maximum dimensions of ice crystals are the same, the ice crystals in the shapes of plates, columns, and hollow columns attenuate more light. The values of IWC are 1.642×10^{-3}, 2.711×10^{-3}, 2.261×10^{-3}, 7.130×10^{-4}, and 5.345×10^{-4} gm^{-3} for plates, columns, hollow columns, bullet rosettes, and aggregates, respectively. The extinction coefficients as a function of wavelength show little variation, except for a minimum feature in 2.85 μm region, the so called Christiansen effect (Arnott et al., 1995). This effect occurs because the real part of refractive index approaches to 1 while the corresponding imaginary part is large, leading to the domination of absorption in light attenuation along with insignificant scattering contribution. For the curves of the calculated single-scattering albedo, deviations for different shapes are observed only in the region 3.7–5 μm. This is because the single-scattering albedo approaches 1 in the spectral region 0.2–2.5 μm due to the weak absorption of ice. In the spectral region near 3 μm, the absorption of ice crystal is essentially saturated with little variation with respect to shapes. It should be pointed out that the minimum of single-scattering albedo near the Christiansen band is much less than 0.5, which cannot be produced by using the conventional ray-tracing technique. The deviations of the asymmetry factor for different shapes are mainly observed in the spectral regions 0.2–2.5 μm and 3.3–5 μm. The values associated with hollow columns are larger than those corresponding to the other shapes, except for the region 0.2–0.6 μm where the plate result exceeds. When the absorption of ice crystal is substantial, the scattered energy is primarily contributed by the diffraction in the forward directions. For this reason, maximum values of the asymmetry factor are noted around 3 μm. It should been noted that the effect of surface roughness is noticeable only for the asymmetry factor.

Figure 13 is similar to Figure 12, except for the size distribution of a warm cirrus that was reported by Heymsfield and Platt (1984). The cutoff of small ice crystals for the size distribution in the single-scattering calculation is at 20 μm. The values of IWC are 1.381×10^{-2}, 2.062×10^{-2}, 1.720×10^{-2}, 6.063×10^{-3}, 1.902×10^{-2} gm^{-3} for plates, columns, hollow columns, bullet rosettes, and aggregates, respectively. Evidently, IWC for the warm cirrus is much larger than the cold cirrus. For this reason, the extinction coefficient for the warm cirrus is also larger. The general features of the single-scattering properties as the functions of wavelength are similar for the two size distributions. However, the computed extinction coefficients for the warm cirrus are almost the same for plates, columns, and hollow columns. In addition, the asymmetry factor associated with plate is substantially larger than those corresponding to the other shapes in the region of 0.2–1.4 μm. It has been demonstrated that the impact of cirrus clouds on climate largely depends on the asymmetry factor value of the phase function associated with ice crystals (Stephens et al., 1990). Macke et al. (1996) have shown that the asymmetry factor for the visible radiation is substantially reduced if an

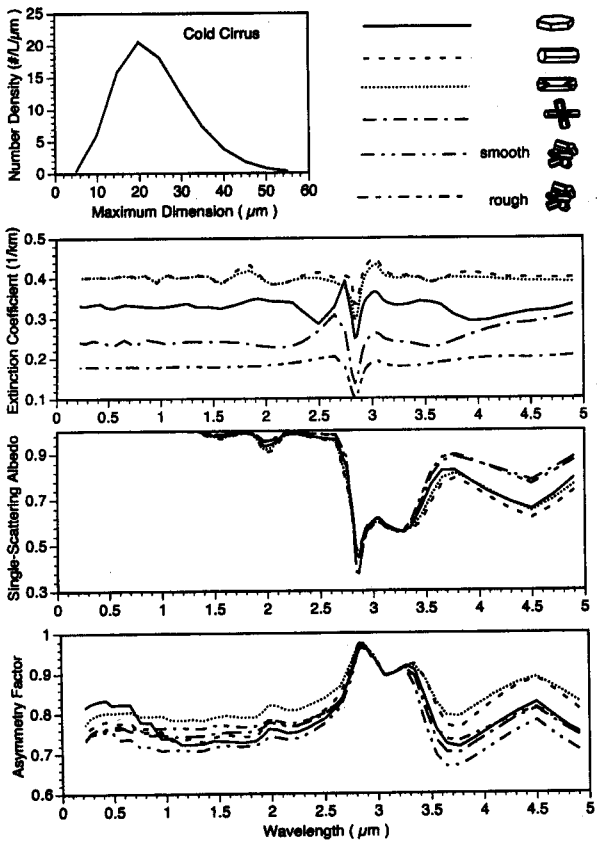

Figure 12: The computed extinction coefficient, single-scattering albedo, and asymmetry factor for a cold cirrus. The size distribution was observed on April 19, 1994 over CART site.

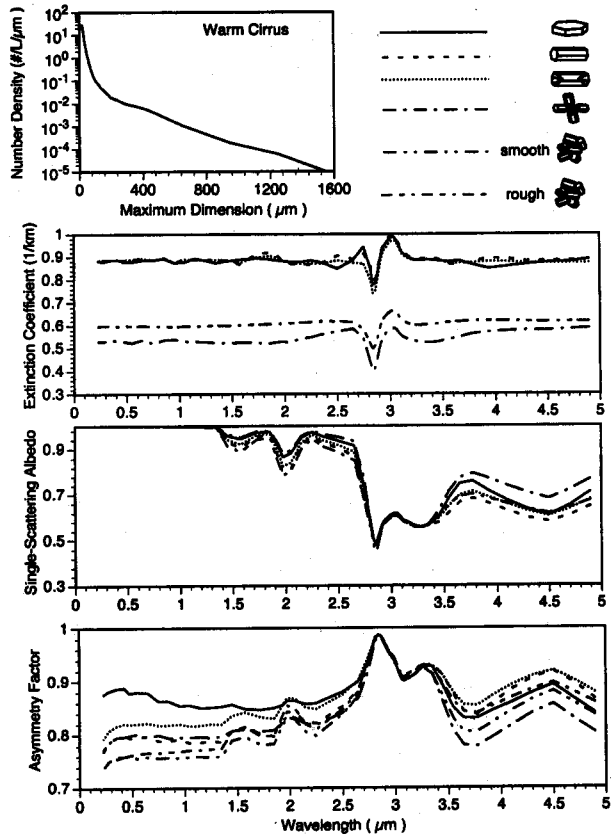

Figure 13: Same as Figure 12, except for a warm cirrus.

ice crystal shape is distorted from a perfect hexagonal structure, as a result of the featureless phase function obtained for a complex ice crystal geometry. This kind of the relevance of the asymmetry factor to ice crystal geometry noted by those authors is in agreement with that shown by the present results. The significance of the reduction for the asymmetry factor in climate implications has been addressed by Mishchenko et al. (1996) and Macke et al. (1996).

According to the results in Figures 12 and 13, it is evident that the bulk single-scattering properties of ice crystals in cirrus clouds depend on both size distribution and ice crystal habit. Thus, the effect of ice crystal shape should be accounted for in the parameterization of the radiative properties of cirrus clouds for an application in climate modeling.

5 Conclusions

Based on replicator ice crystal imagery and the ice crystal shapes observed by Bentley and Humphreys, and Nakaya, various complex crystal geometries have been defined for the ray-tracing calculation. The effect of the surface roughness of ice crystals on the single-scattering properties is also investigated by defining the roughness in terms of Gram Charlier distribution. To comprehensively account for the polarization configuration in the ray-tracing calculation, we have formulated the scattering matrix and the criterion that determines the directions of ray-propagations in conjunction with the Monte Carlo/ray-tracing calculation. In addition, we have also developed an improved diffraction formula for diffraction calculation, in which the polarization of forward diffracted waves and backward propagating waves can be treated properly.

The scattering phase matrix for various complex crystal shapes has been computed using the improved Monte Carlo/ray-tracing algorithm at both visible and near-infrared wavelengths. According to the numerical results, hexagonal ice crystals scatter more energy in angular region from 0° to $\sim$ 1° than com-

plex ice crystals. However, the complex crystals scatter more energy in the lateral and backward directions than their hexagonal counterparts. The magnitude of the degree of linear polarization for the former is significantly smaller for most of the complex geometries defined in this study, especially, for the angular region around the backward scattering direction. The single-scattering properties of the complex crystals may be useful for a better interpretation of the lidar depolarization returns and the polarization of the reflected sunlight from cirrus clouds.

A database of the scattering parameters for various ice crystal shapes and sizes have been established for solar spectrum covering 0.2–5 μm. The corresponding database for infrared wavelengths, computed by a combination of the FDTD technique and the improved geometric optics method, is currently ongoing and will be reported in a future paper. The database provides the fundamental scattering and absorption parameters for a reliable parameterization of the radiative properties of cirrus clouds to account for the effects of size distribution and the percentage of various ice crystal habits. Finally, applying the database to a cold and a warm cirrus, we find that both size distribution and particle shape are important factors in determining the bulk scattering characteristics of ice clouds.

Acknowledgments

We thank Y. Takano for assistance to define the geometry of aggregates. K. Wyser from the University of Stockholm, Sweden assisted the computations in the development of the single-scattering database for various ice crystal shapes and sizes. The authors thank the two anonymous reviewers for constructive comments. This study was supported by U.S. National Sciences Foundation (NSF) grant ATM-93-1521 and in part by NASA grants NAG1-1719, and NAG5-2678, and U.S. Department of Energy (DOE) grant DE-FG03-95ER61991. Some of the computational results presented in this paper were obtained using CRAY Y-MP 8/864 at the National Center for Atmospheric Research, sponsored by NSF.

Appendix: Improved Diffraction Formula

The diffraction matrix obtained by the scalar Fraunhofer diffraction theory for a scattering particle has been extensively employed in previous ray-tracing studies. It can be expressed as follows:

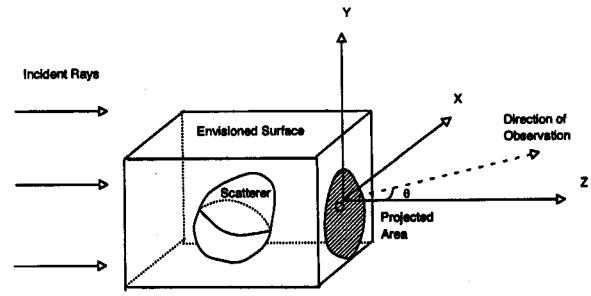

Figure A.1: Geometry for the improved diffraction formula.

$$\mathbf{S}_d = \frac{k^2}{2\pi} D \begin{pmatrix} 1 & 0 \\ 0 & 1 \end{pmatrix}, \tag{A.1}$$

$$D = \iint_P \exp(-ik\hat{r}\cdot\vec{\xi}) d^2\xi, \tag{A.2}$$

where $\hat{r}$ is the scattering direction, and k is the wavenumber. The domain of integration in Eq. (A.2), P, is the projected area of the scattering particle on a screen perpendicular to the incident direction. Evidently, the two polarized components of the diffracted field are assumed to be the same in the scalar formulation. In addition, it should be pointed out that the applicability of the preceding equations must be limited to the scattering angles smaller than 90°; otherwise, a diffraction maximum may be produced incorrectly in the backscattering direction.

To circumvent the disadvantages in the scalar diffraction theory, we consider light scattering by a scatterer that is assumed to be an ideal blackbody, (i.e., the rays impinging on the scatterer are completely absorbed). Thus, the scattered field is essentially caused by the diffraction phenomena due to the presence of the particle. We apply the geometric optics method to solve the near electric field on an envisioned surface which encloses the scatterer, as shown in Figure A.1. Subsequently, the far-field associated with the near-field can be obtained on the basis of the rigorous electromagnetic wave theory. Since the scatterer is a blackbody, the electric field on the envisioned surface in the geometric optics approximation is given by

$$\vec{E}(\vec{r}) = \begin{cases} \vec{E}^i(\vec{r}), & \vec{r} \notin \text{projected area} \\ 0, & \vec{r} \in \text{projected area} \end{cases}, \tag{A.3}$$

where $\vec{E}^i(\vec{r})$ is the incident field, and the projected area is the projection of the scatterer on the envisioned surface along the incident direction, as shown in Figure A.1. According to electromagnetic principles, we can express the scattered far-field as follows (Yang and Liou, 1996b):

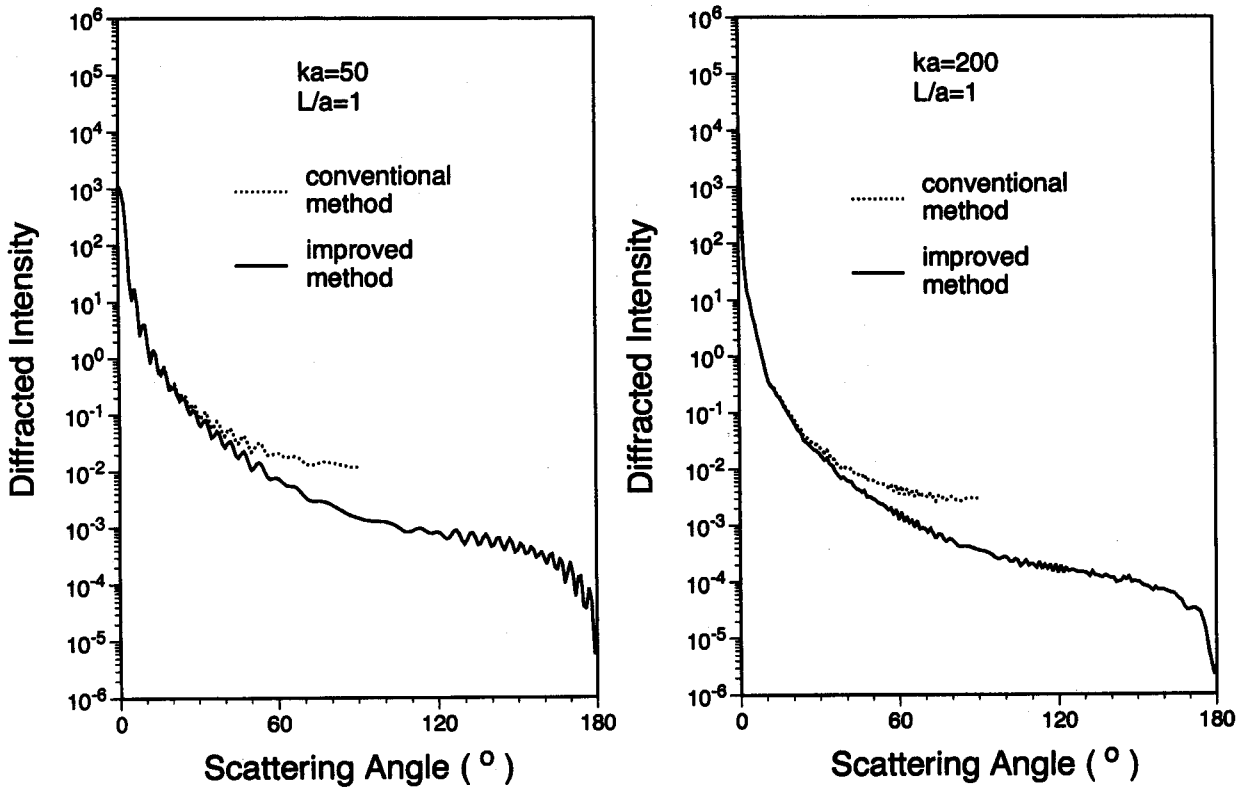

Figure A.2: Diffracted intensity computed from the scalar diffraction theory and the present improved method for randomly oriented hexagons.

$$\vec{E}^s(\vec{r}) = \frac{e^{ikr}}{-ikr}\frac{k^2}{4\pi}\hat{r}\times\left\{\hat{r}\times\left[\oiint_s[\hat{n}_s\cdot\hat{r}\vec{E}(\vec{\xi}) + \frac{1}{ik}\frac{\partial\vec{E}(\vec{\xi})}{\partial n_s}\right]e^{-ik\hat{r}\cdot\vec{\xi}}d^2\xi\right\}$$

$$= \frac{e^{ikr}}{-ikr}\frac{k^2}{4\pi}\hat{r}\times\left\{\hat{r}\times\left[\oiint_s - \iint_P\right]\right.$$

$$\left.[\hat{n}_s\cdot\hat{r}\vec{E}^i(\vec{\xi}) + \frac{1}{ik}\frac{\partial\vec{E}^i(\vec{\xi})}{\partial n_s}]e^{-ik\hat{r}\cdot\vec{\xi}}d^2\xi\right\}, \qquad \text{(A.4)}$$

where $\hat{r}$ is the scattering direction, $\hat{n}_s$ is the outward normal direction of the surface, and the domain of integration, s, is the whole envisioned surface. It can be proved that the integration of the incident wave over the envisioned surface is zero. Thus, using Eq. (A.4) and referring to the geometry in Figure A.1, we obtain the following relationship:

$$\vec{E}^s(\vec{r}) = \frac{e^{ikr}}{ikr}\frac{k^2}{4\pi}\hat{r}\times\left\{\hat{r}\times\iint_P[\hat{n}_s\cdot\hat{r}\vec{E}^i(\vec{\xi}) + \frac{1}{ik}\frac{\partial\vec{E}^i(\vec{\xi})}{\partial n_s}]e^{-ik\hat{r}\cdot\vec{\xi}}d^2\xi\right\}$$

$$= \frac{e^{ikr}}{ikr}\frac{k^2}{4\pi}[\hat{e}_z\cdot(\hat{r}+\hat{e}_z)]\hat{r}\times(\hat{r}\times\vec{A})D$$

$$= \frac{e^{ikr}}{ikr}\frac{k^2}{4\pi}\hat{r}\times(\hat{r}\times\vec{A})D(1+\cos\theta), \qquad \text{(A.5)}$$

where $\vec{A}$ is the amplitude of the incident electric field. After decomposing the scattered and incident fields into two components parallel and perpendicular to the scattering plane, we obtain the amplitude scattering matrix associated with the diffraction contribution as follows:

$$\mathbf{S}_d = \frac{k^2D}{4\pi}\begin{bmatrix}\cos\theta+\cos^2\theta & 0\\ 0 & 1+\cos\theta\end{bmatrix}, \qquad \text{(A.6)}$$

where D is defined in Eq. (A.2), and θ is the scattering angle. Because the scattering matrix $\mathbf{S}_d$ is determined by the particle projection other than the particle geometry in the 3-D space, it is evident that diffraction of the scatterer is equivalent to that of an aperture that

has exactly the same shape as the projected area of the scatterer. This is essentially the Babinet's principle (van de Hulst, 1957; Born and Wolf, 1959) but the vector property of the electromagnetic wave is included in the present formulation. Unlike in the scalar diffraction theory of the conventional geometric optics, the backward propagating diffracted wave (for scattering angles larger than 90°) can be solved by using Eq. (A.6) because of the inclusion of an angular factor, $\cos\theta$. Furthermore, it should be pointed out that the polarization configuration of the diffracted wave computed from the improved diffraction formulation can differ from that of the incident wave because the two nonzero matrix-elements of $\mathbf{S}_d$ defined in Eq. (A.6) are not identical. Thus, a depolarization associated with diffraction phenomena can be produced for an incident beam of linearly polarized light according to the present method, which cannot be obtained from the conventional scalar diffraction theory, however.

Figure A.2 illustrates the comparison of the diffracted intensity values associated with randomly oriented hexagons, which are computed by the conventional scalar diffracted theory and the present method. A concise and efficient formulation can be derived for the diffraction integration involved in Eq. (A.2) by using the symmetry of a hexagon, although this integration has been solved by Cai and Liou (1982) and Takano and Asano (1983). The projection of a hexagonal ice crystal on an opaque screen perpendicular to the incident direction is an octagon. Defining the eight apexes of the octagon to be (x_i,y_i), $i = 1-8$, and noting the symmetric relationship of $(x_{i+4},y_{i+4}) = -(x_i,y_i)$, $i = 1-4$, we obtain

$$D = \sum_{i=1}^{3} 2\sigma_i \frac{(\cos q_i - 1)/q_i - (\cos q_{i+1} - 1)/q_{i+1}}{q_{i+1} - q_i} - 2\sigma_4 \frac{(\cos q_4 - 1)/q_4 + (\cos q_1 - 1)/q_1}{q_1 + q_4}, \quad \text{(A.7)}$$

$$\sigma_i = | x'_i y'_{i+1} - x'_{i+1} y'_i |, i = 1,2,3, \quad \text{(A.8)}$$

$$\sigma_4 = | x'_1 y'_4 - x'_4 y'_1 |, \quad \text{(A.9)}$$

$$q_i = k \sin\theta (x'_i \cos\varphi + y'_i \sin\varphi), i = 1-4, \quad \text{(A.10)}$$

where θ and φ are the scattering zenith and azimuthal angles. As shown in Figure A.2, the computation of the diffracted wave obtained from the conventional method is confined to the scattering angles smaller than 90° due to the inability of the method in dealing with the backward propagating waves. This kind of computational discontinuity is removed in the new method. For the scattering angles larger than 20°, the values computed from the conventional theory are larger than those computed from the new method. For large size parameters, such as ka=200, the diffracted energy is mainly concentrated in a very narrow region around the forward scattering direction, thus, the difference between the two methods is not significant in terms of the amount of energy.

References

Ackerman T.P., Liou, K.N., Valero, F.P.J., and Pfiste, L., 1988: Heating rates in tropical anvils. J. Atmos. Sci. **45**, 1606–1623.

Arnott W.P., Dong Y.Y., and Hallett J., 1995: Extinction efficiency in the infrared (2–18 μm) of laboratory ice clouds: Observation of scattering minima in the Christiansen bands of ice. Appl. Opt. **34**, 541–551.

Auer A.H.Jr. and Veal D.L., 1970: The dimension of ice crystals in natural clouds. J. Atmos. Sci. **27**, 919–926.

Bentley W.A. and Humphreys W.J., 1962: Snow crystals. Dover, New York, 227pp.

Bretherton F.P. and Suomi V.E., 1983: First Internal Satellite Cloud Climatology Project Regional Experiment (FIRE) Research Plan. 76pp. [Available from the National Climatic Program Office, Rm. 108, 11400 Rockville Pike, Rockville, MD 20852].

Born M. and Wolf E., 1959: Principles of Optics, Pergamon, New York, 803pp.

Cai Q. and Liou K.N., 1982: Polarized light scattering by hexagonal ice crystals: Theory. Appl. Opt. **21**, 3569–3580.

Coleman R.F. and Liou K.N., 1981: Light scattering by hexagonal ice crystals. J. Atmos. Sci. **38**, 1260–1271.

Cox C. and Munk W., 1954: Measurement of the roughness of the sea surface from photographs of the sun's glitter. J. Opt. Amer. Soc. **44**, 838–850.

Cross J.D., 1968: Study of the surface of ice with a scanning electron microscope. Physics of Ice, Proceeding of International Symposium on Physics of Ice, Munich, Germany, September 9–14, 1968. Plenum Press, New York, 81–94.

Ebert E.E. and Curry J.A., 1992: A parameterization of ice cloud optical properties for climate models. J. Geophys. Res. **97**, 3831–3836.

Flatau P.J., Stephens G.L., and Draine B.T., 1990: Light scattering by rectangular solids in the discrete-dipole approximation: a new algorithm exploring the block-toeplitz structure. J. Opt. Soc. Am. A **7**, 593–600.

Fu Q., 1996: An accurate parameterization of the solar radiative properties of cirrus clouds for climate models. J. Climate, **9**, 1996.

Fu Q. and Liou K.N., 1993: Parameterization of the radiative properties of cirrus clouds. J. Atmos. Sci. **50**, 2008–2025.

Gayet J.E., Febvre G., and Larson P., 1996: The reliability of the PMS FSSP in the presence of small ice crystals. J. Atmos. Ocean. Tech. **13**, 1300–1310.

Goedecke G.H., and O'Brien S.G., 1988: Scattering by irregular inhomogenous particles via the digitized Greens's function algorithm. Apll. Opt. **27**, 2431–2438.

Gosse S., Labrie D., and Chylek P., 1995: Refractive index of ice in the 1.4 to 7.8 μm spectral range. Appl. Opt. **34**, 6582-6586.

Greenler R.G., 1980: Rainbows, Halos, and Glories. Cambridge University Press, New York, 195pp.

Heymsfield A.J. and Platt, C.M.R., 1984: A parameterization of the particle size spectrum of ice clouds in terms of the ambient temperature and the ice water content. J. Atmos. Sci. **41**, 846–855.

Hobbs P., 1974: Ice Physics. Oxford University Press, Bristol, England, 837pp.

van de Hulst H., 1957: Light Scattering by small particles. Dover, New York, 470pp.

Iaquinta J., Isaka H., and Personne P., 1995: Scattering phase function of bullet rosette ice crystals. J. Atmos. Sci. **52**, 1401–1413.

Kinne S. and Liou K.N., 1989: The effects of the nonsphericity and size distribution of ice crystals on the radiative properties of cirrus clouds. Atmos. Res. **24**, 273–284.

Kinne S., Bergstrom R., Ackerman T.P., Heymsfield A.J., Deluisi J., Shiobara M., Pilewskie P., Valero F.P.J., and Takano Y., 1994: Cirrus cloud solar radiative properties: comparisons between theory and observations based measurements during FIRE'91. Prepints of Eighth Conference on Atmospheric Radiation, January 23–28, Nashville, Tennessee, Amer. Meteor. Soc., 418–420.

Kneizys F.X. and co-authors, 1988: Users guide to LOWTRAN7, Environmental Research Papers, No. 1010, Air Force Geophysics Laboratory, Hanscom AFB, MA.

Liou K.N., 1986: Influence of cirrus clouds on weather and climate processes: A global perspective. Mon. Wea. Rev. **114**, 1167–1199.

Liou K.N. and Takano Y., 1994: Light scattering by nonspherical particles: Remote sensing and climatic implications. Atmos. Res. **31**, 271–298.

Lux I. and Koblinger L., 1991: Monte Carlo particle transport methods: Neutron and photon calculations. CPC Press, Boca Raton, Florida, 517pp.

Macke A. and Tzschihholz F., 1992: Scattering of light by fractal ice particles: A qualitative estimate exemplary for two-dimensional triadic Koch-island. Physica A**191**, 159–170.

Macke A., 1993: Scattering of light by polyhedral ice crystals. Appl. Opt. **32**, 2780-2788.

Macke A., Mishchenko M.I., Muinonen, and Carlson B.E., 1995: Scattering of light by large nonspherical particles: ray-tracing approximation versus T-matrix method. Opt. Lett. **20**, 1934–1936.

Macke A., Muller J., and Rascke E., 1996: Single scattering properties of atmospheric crystals. J. Atmos. Sci. **53**, 2813–2825.

Magano C., and Lee C., 1966: Meteorological classification of natural snow crystals. J. Fac. Sci. Hokkaido Univ. **Ser VII 2**, 321–335.

Mandelbrot B., 1982: The fractal geometry of nature. W.H. Freeman and Co., San Francisco, CA, 460pp.

Minnis P., Young D.F., Garber D.P., Takano Y., and Liou K.N., 1994: Effect of cloud particle size and shape on satellite remote sensing of cloud properties. Prepints of Eighth Conference on Atmospheric Radiation, January 23-28, Nashville, Tennessee, Amer. Meteor. Soc., 418–420.

Mishchenko M.I., 1993: Light scattering by size-shape distributions of randomly oriented axially symmetric particles of a size comparable to a wavelength. Appl. Opt. **32**, 4652–4666.

Mishchenko M.I., Rossow W.B., Macke A., and Lacis A.A., 1996: Sensitivity of cirrus cloud albedo, bidirectional reflectance and optical thickness retrieval accuracy to ice particle shape. J. Geophys. Res. **101**, 16973–16985.

Mitchell D.L. and Arnott W.P., 1994: A model predicting the evolution of ice particle size spectra and radiative properties of cirrus clouds. Part II: Dependence of absorption and extinction on ice crystal morphology. J. Atmos. Sci. **51**, 817–832.

Mitchell D.L., Chai S.K., Liu Y., Heymsfield A., and Dong Y., 1996: Modeling cirrus clouds. Part I: Treatment of bimodal size spectra and case study analysis. J. Atmos. Sci. **53**, 2952–2966.

Muinonen K., 1989: Scattering of light by crystals: A modified Kirchhof approximation. Appl. Opt. **28**, 3044–3050.

Muinonen K., Nousiainen T., Fast P., Lumme K., and Peltoniemi J.I., 1996: Light scattering by Gaussian random particles: Ray optics approximation. J. Quant. Spectrosc. Radiat. Transfer, **55**, 577–613.

Nakaya U., 1954: Snow Crystals. Harvard University Press, Cambridge, 510pp.

Ono A., 1969: The shape and riming properties of ice crystals in natural clouds. J. Atmos. Sci. **26**, 138–147.

Peltoniemi J.I., Lumme K., Muinonen K., and Irvine W.M., 1989: Scattering of light by stochastically rough particles. Appl. Opt. **28**, 4088–4095.

Purcell E.M. and Pennypacker C.P., 1973: Scattering and absorption of light by nonspherical dielectric grains. Astrophys. J. **196**, 705–714.

Ramaswamy V. and Ramanathan V., 1989: Solar absorption by cirrus clouds and the maintenance of the tropical upper troposphere thermal structure. J. Atmos. Sci. **46**, 2293–2310.

Rockwitz K.D., 1989: Scattering properties of horizontal oriented ice crystal columns in cirrus clouds. Part I. Appl. Opt. **28**, 4103–4110.

Santer R., Deschamps M., Ksanfomaliti L.V., and Dollfus A., 1985: Photopolarimetric analyses of the Martian atmosphere by the Soviet MARS-5 orbitar. Astron. Astrophys. **150**, 217–228.

Stephens G.L., Tsay S., Stackhouse P.W.Jr., and Flatau P.J., 1990: The relevance of the microphysical and radiative properties of cirrus clouds to climate and climate feedback. J. Atmos. Sci. **47**, 1742–1753.

Takano Y. and Asano S., 1983: Fraunhofer diffraction by ice crystals suspended in the atmosphere. J. Meteo. Soc. Japan, **61**, 289–300.

Takano Y. and Jayaweera K, 1985: Scattering phase matrix for hexagonal ice crystals computed from ray-tracing. Appl. Opt. **24**, 3254–3263.

Takano Y. and Liou K.N., 1989a: Solar radiative transfer in cirrus clouds. Part I: Single-scattering and optical properties of hexagonal ice crystals. J. Atmos. Sci. **46**, 3–19.

Takano Y. and Liou K.N., 1989b: Solar radiative transfer in cirrus clouds. Part II: Theory and computation of multiple scattering in an anisotropic medium. J. Atmos. Sci. **46**, 20–36.

Takano Y. and Liou K.N., 1995: Radiative transfer in cirrus clouds. Part III: Light scattering by irregular ice crystals. J. Atmos. Sci. **52**, 818–837.

Umashankar K. and Taflove A., 1982: A novel method to analyze electromagnetic scattering of complex objects. IEEE Trans. Electromagn. Compat. **EMC-24**, 397-405.

Vicsek T., 1989: Fractal growth phenomena. World Scientific, Singapore, 355pp.

Warren S.G., 1984: Optical constants of ice from the ultraviolet to the microwave. Appl. Opt. **23**, 1206–1225.

Wendling P., Wendling R., and Weickmann H.K., 1979: Scattering of solar radiation by hexagonal ice crystal. Appl. Opt. **18**, 2663–2671.

Wielaard J., Mishchenko M.I., Macke A., and Carlson B., 1997: Improved T-matrix computations for large, nonspherical and weak absorbing nonspherical particles and comparison with geometrical-optics approximation. Appl. Opt. **36**, 4305–4313.

Witten T.A. and Sander L.M., 1983: Diffusion-limited aggregation. Phys. Rev. **27**, 5686–5697.

Wylie D.P. and Menzel W.P., 1989: Two years of cloud cover statistics using VAS. J. Climate **2**, 380–392.

Yang P. and Liou K.N., 1995: Light scattering by hexagonal ice crystals: comparison of finite-difference time domain and geometric optics models. J. Opt. Soc. Am. A **12**, 162–176.

Yang P. and Liou K.N., 1996a: Finite-difference time-domain method for light scattering by small ice crystals in three dimensional space. J. Opt. Soc. Am. A **13**, 2072–2085.

Yang P. and Liou K.N., 1996b: Geometric-optics-integral-equation method for light scattering by nonspherical ice crystals. Appl. Opt. **35**, 6568–6584.

Yang P. and Liou K.N., 1997: Light scattering by hexagonal ice crystals: solution by a ray-by-ray integration algorithm. J. Opt. Soc. Am. A **14**, 2278–2288.

Yang P., Liou K.N., and Arnott W.P., 1997: Extinction efficiency and single-scattering albedo for laboratory and natural cirrus clouds. J. Geophys. Res. **102**, 21825–21835.

Zerull R.H., Giese R.H., Schwill S., and Weiss K., 1980: Scattering by particles of non-spherical shape. In: Schuerman D.W. (ed), Light scattering by irregularly shaped particles, Plenum Press, 273–283.

Zhang J. and Xu L., 1995: Light scattering by absorbing hexagonal ice crystals in cirrus clouds. Appl. Opt. **34**, 5867–5874.

Zuffada C. and Crisp D., 1997: Particle scattering in the resonance regime: full-wave solution for axisymmetric particles with large aspect ratios. J. Opt. Soc. Am. A **14**, 459–474.